

TW5-TTMS-004-D02

Task Title: QUALIFICATION FABRICATION PROCESSES MICROSTRUCTURAL ANALYSIS AND QUALIFICATION OF JOINTS AND WELDS FROM TBM MOCK-UP FABRICATION

INTRODUCTION

Eurofer weldability must be established for data base assessment on such low activation martensitic steel. Electron Beam, Hybrid (Laser combined with MIG/MAG), Laser and TIG processes have been carried out on Eurofer samples from 8 mm to 40 mm. Joint design tested are the same than those developed in TW2-TTBC-002-D02 manufacturing task. This report will set up metallurgical behaviour for each welding configuration and a result comparison for all processes carried out.

2006 ACTIVITIES

The TBM modules require a large number of Eurofer welds for a complex structure. The weldability must be assessed on real joint configurations on the second batch of Eurofer. Electron beam, Hybrid (MIG/Laser), TIG and Laser welding processes have been applied on flat samples. Welding operating conditions are optimised in the stationary stage to process sound joints. Welding configurations are divided in two sketches, as following:

- Electron Beam and Hybrid: thickness 25 to 40 mm,
- YAG Laser and TIG: 8 mm (4 mm on both sides).

Welding requirements are sound structural welds, free of cracks with high joint coefficient and low pores level. Mechanical weld performances of this report will feed TBM code work for RCCMR codes requirements.

WELDING CONFIGURATION DESCRIPTION

TBM module is a very complex sub-assembly to manufacture. A lot of welding to perform this complex unit is presented in the following lines and figure 1.

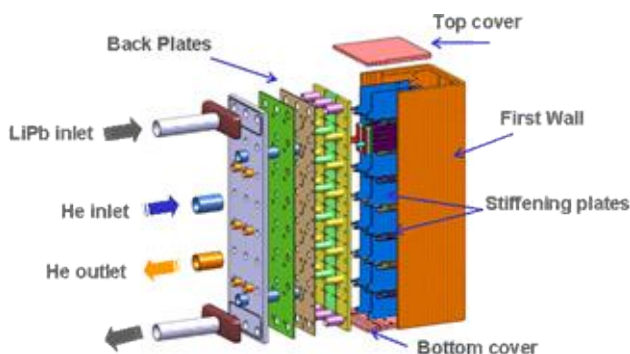
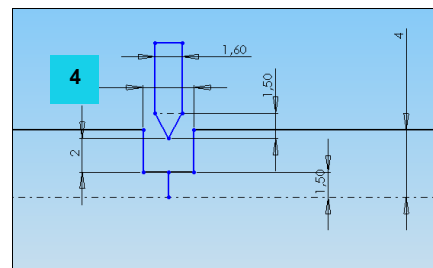


Figure 1: TBM design

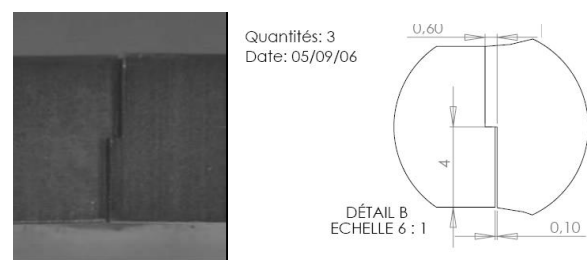
Coming from the design and welding development stage on TW2-TTBC-002-D02 task, the following welding configurations have been processed on flat samples, in full or EDM machining channels plates, for getting metallurgical behaviour the closer as possible from real TBM design.

Welding configuration 1: Horizontal Stiffening Plate / Vertical Stiffening Plate

TIG and Laser Joining processes have been tested. For TIG and Laser process, specific joint geometries have been developed. Metallurgical behaviour has been analyzed for butt joints welding configuration on and real joint geometries, which have been assessed in TW2-TTBC-002-D02 task, as shown in figure 2.



TIG joint design



Laser joint geometry

Figure 2: Developed joint geometries

Joint requirements:

- Only one horizontal plate's row out of two is welded in this step; the other rows are welded after welding of the grid on the first wall.
- 214 mm between horizontal plates, and 180 mm between vertical plates.
- Very low distortion allowed for positioning on the first wall / side walls and breeder units insertion.

The stiffening grid is used to insure the mechanical withstanding of the module in case of internal accidental pressure. Welding failure may lead to unacceptable damages.

Welding configuration 3: covers on the first wall / side walls

Former works performed on Eurofer and F82H steels, hot cracks have been observed on EB process. So, a second welding process has been carried out: Hybrid (laser/MIG) process, through CEA welding experience and knowledge. Narrow Gap TIG Welding (NGTIG) could have been taken in account, but this process presents quite the same welding behaviour than Hybrid process and produces more high distortion level. NGTIG is considered as “safety belt” process, safe in processing but providing too many distortions. The groove design of Hybrid process is shown in figure 3.

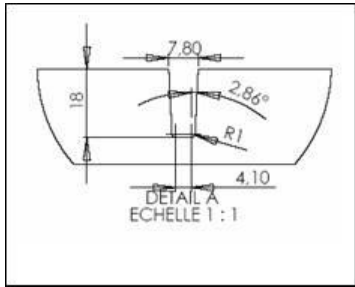


Figure 3: Hybrid process groove design

In summary, two welding configurations must be analyzed:

- 8 mm thickness butt or edge joint: TIG or Laser process.
- 17 to 40 mm thickness butt or edge joint: EB or Hybrid process.

Welding requirements are sound structural welds, free of cracks with high joint coefficient and low pores level.

HYBRID WELDING

The MIG/laser hybrid process technology developed in several ITER tasks on vacuum vessel has been fully applied on Eurofer 25 mm thickness plates. For the following welding trials, a Eurofer standard filler wire, 1 mm diameter, has been used for hybrid joining tests, with chemical composition quite the same than the base material.

Two different welding conditions have been carried out on 400 x 300 x 20 mm³ samples. The first weld 06P014-1-1 has been performed, without pre-heating and post-heating treatment, with no waiting time and no joint cleaning between each filling pass. For filling the joint groove, 14 filling passes were realized. The second one 06P014-1-2 has been processed with a 200°C pre-heating and post-heating during 2 hours at 300°C. Welding deposit rate is about 3.7 kg/hour for a welding travel speed of 0.8 m/min and a filler wire speed of 10 m/min with a wire diameter of 1 mm. The welds obtained for each welding pass have good external aspect without oxidation.

On each welded joint, transverse cross sections have been made (figure 4). Hybrid welds looks homogeneous and its borderlines quite nearly parallel. No defect such sticking, is observed and only few pores (0.3 mm diameter). It shows good weld geometry and the side wall penetration depth measured is in the range of 0.5 to 1 mm same results are observed on the second sample 06P014-1-2. Hybrid welds

show coarse grain formation in the fusion zone. Equiaxed grains with 20 μm grain size of martensite laths are fully produced in all welds, which is twice the base material grain size (12 μm). No δ ferrite and carbides have been observed in the fusion zone. Micrographs cross sections are presented in figure 5.

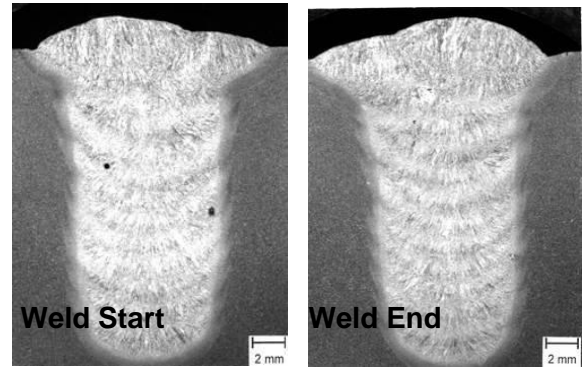
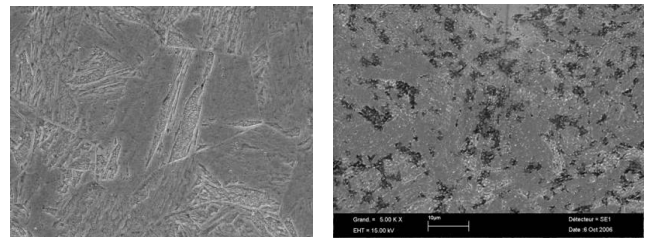


Figure 4: Hybrid transverse macrographs



Fusion zone microstructure HAZ microstructure
Figure 5: Hybrid welds microstructure

No difference in the Fusion Zone between the two welding conditions with and without pre- and post-heating treatment is observed: same microstructure and grain size. Coarse grain zone can be observed in the zone where the layer of the former welding pass is affected by following one. In Heat Affected zone (HAZ), the microstructure is on type fine martensite grains with fine M₂₃C₆ carbide precipitates which are small size white points on figure 4. Compared to the base material the grain size is smaller in the HAZ by about a factor of 2. HAZ is driven by α → β transformation fully martensitic, with smaller grain size than in base material, and carbide coalescence.

Profile Hardness

Maximum hardness level is observed in the fusion zones. It varies between 410 and 490, explained by the multi-pass welding procedure (figure 6).

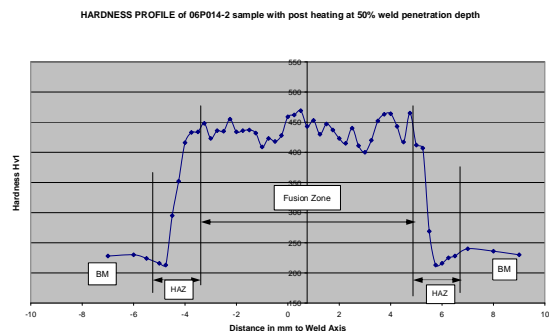


Figure 6: HVI profile hardness

The influence of the 200°C pre -and post-heating is too low for reducing these hardness fluctuations. The hardness average level in fusion zone is too high for both welds and will reduce strongly weld ductility and fatigue behaviour which shows the necessity of a high temperature PWHT treatment, to restore good weld properties.

ELECTRON BEAM WELDING

Electron Beam process (EB) is also foreseen in high depth welding. The following welding parameters have been applied: High voltage: 150 kV, Welding current: 72 mA, Travel speed: 0.3 m/min (figure 7).

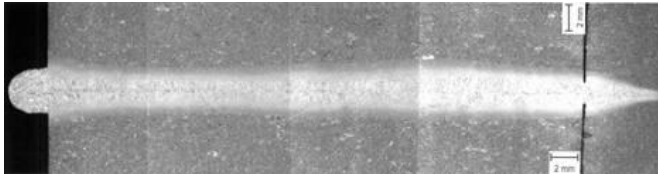


Figure 7: Macrograph cross section of EB weld

The thickness sample is 40 mm and weld width 2 mm. There is no defect inside the weld, free of cracks, bubbles and inclusions. It has been observed δ ferrite apparition. The δ ferrite indicates a too much high cooling rate, which explains coarse grain and high hardening level in the fusion zone.

The grain size of EB weld fusion zone is small: 20 to 30 μm , a little bit greater than Hybrid welds, due to the higher welding energy injected to produce a 40 mm penetration depth, to compare with 2 mm in multi-pass Hybrid welds. Fusion zone exhibits a strongly disordered coarse grain weld zone (figure 8).

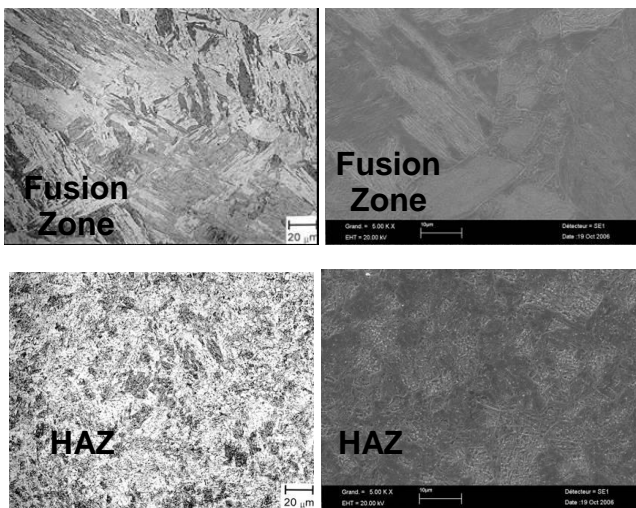


Figure 8: Micrograph cross section of EB weld

The hardness profile of Electron Beam weld at mid penetration depth is given in figure 9.

The same metallurgical behaviour is observed in EB and Hybrid welds: same microstructure in Fusion Zones and Heat Affected Zone, hardening in fusion zone, hardness decreasing in HAZ compared to base material, same level of hardness value. The very narrow EB width of fusion zone and HAZ will enhance metallurgical and mechanical

troubles. The δ ferrite is observed only in EB weld. Selection of welding process will come only from manufacturing analysis. For both welding processes, PWHT definition seems to be important to develop.

EUROFER 97 Electron Beam Welding PROFILE HARDNESS at half penetration depth

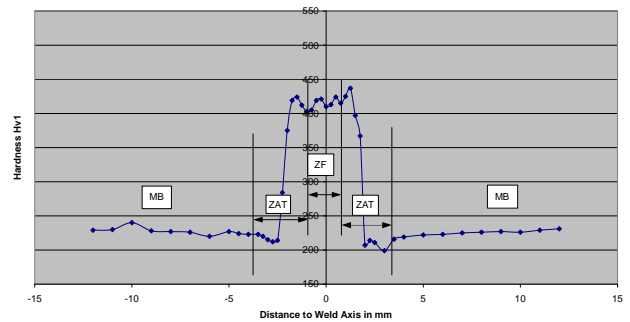


Figure 9: HVI profile hardness of EB weld

TIG WELDING

TIG welding experiments have been processed on flat samples with a standard welding torch equipped with a 1.6 mm diameter tungsten electrode on flat samples. These welding tests have permitted to develop TIG welding process, waiting the specific low size torch providing. The same coil of filler wire than Hybrid process experiments has been used. It has been determined 3 welding passes for each side of the 8 mm horizontal Stiffening Grid, which lead to 6 welding, passes for this whole joining: 2 root passes (1 for each side) and 4 filling passes. Each pass is in a range of 1.5 mm penetration depth, to reduce distortions in decreasing welding energy and weld width. It requires a TIG welding intensity for the welding torch in the range of 160 A, compatible with a TIG torch of 14 mm diameter (figure 10).

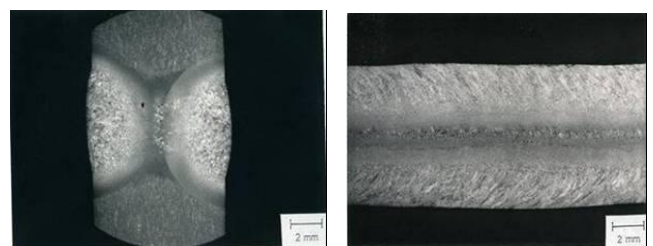
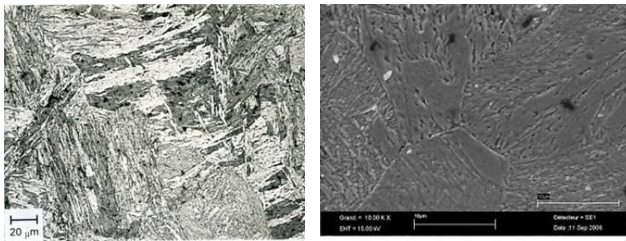
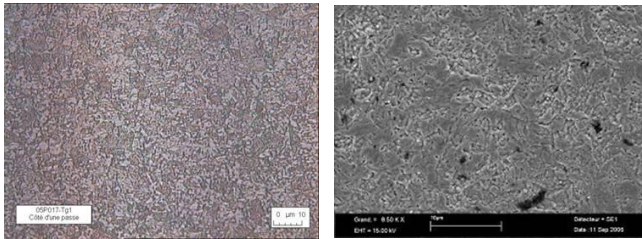


Figure 10: TIG final welds cross and longitudinal sections

In the fusion zone, equiaxe grains of martensite laths are fully produced. No δ ferrite has been observed in the fusion zone. So, no defect welding deviation of TIG arc will be expected, due to a possible magnetic field. Grain size in fusion zone is quite irregular and in the range of 40 μm to 100 μm , which is twice to four times the base material grain size (20 μm). No defects like cracks and inclusions are observed in the welds. Compared to the base material, the grain size of the HAZ is smaller by about a factor of two, and on type fine martensite with fine M_{23}C_6 carbide precipitates. HAZ is driven by $\alpha \rightarrow \beta$ transformation fully martensitic, with smaller grain size than in base material, and carbide coalescence (figure 11).



TIG Fusion Zone



TIG welds Heat Affected Zone

Figure 11: Multi-pass TIG weld microstructure

Heat Affected Zone width for TIG welds is in the range of 3 mm, which is quite huge, and the base material will be affected around the first cooling channel on the horizontal Stiffening Grid plate and on the edge of the vertical plate. The distance between the weld axis position to the first wall of the cooling channel number 1 has been designed with a distance of 3 mm value (A). Fusion Zone (FZ) has a width of 7 mm for TIG process. So, total width from weld axis affected by TIG welding process can be estimated to 5.5 mm Flat samples with EDM channels (100 x 100 x 8 mm³) have been welded with a distance A = 5 mm. Cross sections of such welds are presented in figure 12. It shows the surface modification of the internal face of the cooling channel, due to very high stress level. However, it has been observed no crack but only distortions. The evident conclusion is that A = 5 mm distance must be implemented to minimum 7 mm, for the cooling channel position. The stress concentration level in this area: HAZ for TIG weld must be taken in account in the development of the PWHT process to reduce strain, hardness level and carbide precipitation (fine M₂₃C₆ carbide precipitates) in this specific area.

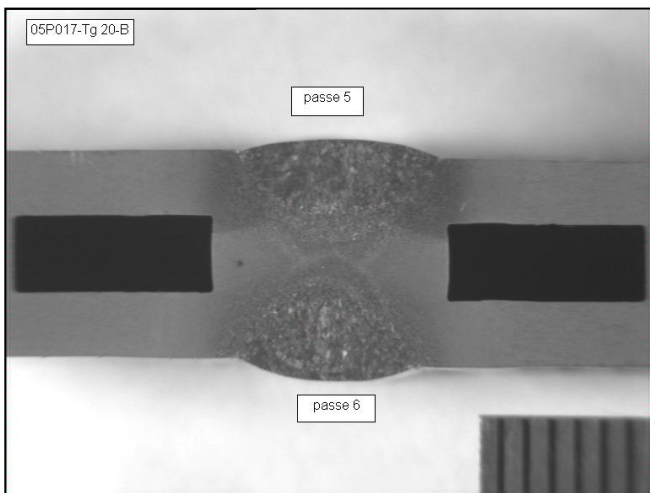


Figure 12: TIG welds cross section with A = 5 mm distance and EDM channels

TIG hardness profile

These profiles have been operated on the two types of samples, without and with EDM cooling channels. The average level for Fusion Zone is in the range of 436 HV_{0.5}, which is an increasing of 205 HV_{0.5} compared to the base material, and small decreasing in Heat Affected Zone (figure 13). Hardness reducing effect in HAZ is related to carbide formation (fine M₂₃C₆ carbide precipitates). Average level of hardness is a little smaller for samples with channels in comparison to full flat samples (around 10%). Maximum hardness is observed in the fusion zones. The hardness average level in fusion zone is too high for both welds and will reduce strongly weld ductility and fatigue behaviour.

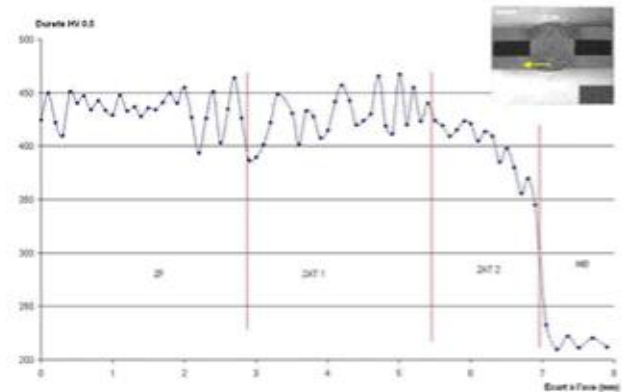


Figure 13: Hardness profile of flat samples TIG welds

Laser welding

Laser process induces less welding distortions than the other welding processes. Cross section (figure 14) illustrates quite good weld aspects. Few pores are observed and also no trouble in the overlapping of the two welds pass. Figure 14 illustrates the very fine structures observed in base material and fusion zone: martensite total transformation is observed with carbide ferritic matrix.

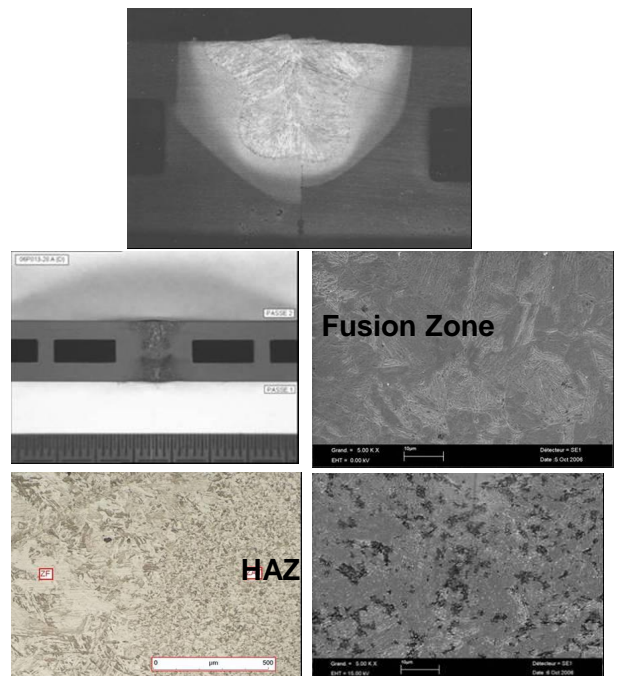


Figure 14: Transverse and longitudinal cross section

Former austenite grain size is estimated to 6 - 8 μm . Martensite laths are observed in Fusion Zone with former austenite grain size in range 20 to 30 μm . The grain size of laser weld Fusion Zone is small: 10 to 20 μm , in the same range than hybrid welds and rather smaller than TIG welds 40 μm to 100 μm and base material (20 μm). Fusion Zone exhibits a strongly coarse grain weld zone. Equiaxed grains of martensite laths are fully produced. No δ ferrite has been observed in the fusion zone.

HAZ microstructures present fine martensite, no δ ferrite, fine grains smaller with a factor of 2 to 3, compared to fusion zone. HAZ width at 50% welds penetration depth is in the range of 0.5 mm, which is quite low and 3 times smaller than TIG process. Small white points in high magnification rate of HAZ cross sections are carbide precipitation (fine M_{23}C_6 carbide precipitates), which will lead to a hardness reduction in HAZ, compared to base material.

Profile Hardness

Profile hardness for laser mono spot welding is shown in figure 15. The hardness average level in laser Fusion Zone is very high: around 455 $\text{HV}_{0.5}$ and 360 $\text{HV}_{0.5}$ in HAZ.

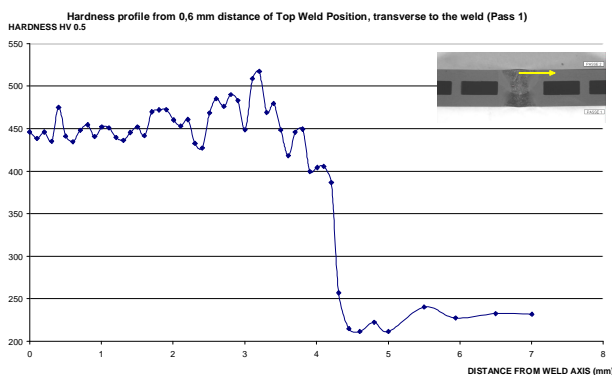


Figure 15: Laser weld hardness profile (Pass 1)

The limits of HAZ did not reach the corners of the first cooling channel. There is no distortion of the shape of this channel. The laser weld microstructures are quite the same than those observed in full plate samples. Fusion Zone width at top part of the weld is in the range of 6.8 mm, i.e. 3.4 mm from weld axis. In comparison, for the same welds, the Fusion Zone width is around 7.6 mm. At 4 mm from the weld axis, the welded plate recovers the hardness of the base material (figure 15). This indication shows no effect on the first cooling channel, which was not the result from TIG welds, which have affected in terms of distortions and strains concentration this channel. The average level of hardness profile in Fusion Zone is quite the same for the two laser welding passes. The fluctuations are high in this coarse and brittle area. It has been explained in hybrid weld tests in the former lines that a high temperature pre- and post-heating treatment (around 400°C – 450°C) during laser welding can:

- Reduce strongly hardness level in Fusion Zone,
- Decrease hardness fluctuations in Fusion Zone.

However, this heat treatment will complicate strongly the laser welding procedure and clamping device conception.

CONCLUSIONS

Electron Beam process is not well adapted for this application. Processing troubles have been demonstrated: too narrow Fusion Zone and HAZ width, δ ferrite content, and too high hardness level gradient. Interesting results have been got using the MIG/laser Hybrid technique developed by CEA. Six TIG welding passes are necessary, compared to the 2 passes for laser process. High hardness level in Fusion Zone and carbide formation in HAZ let think to apply PWHT process or even pre- and post-heating process. Horizontal / Vertical Stiffening Grid mock-ups have been performed. Laser process is reference process, and TIG is second hand process. Distortion level performed by laser process is acceptable for manufacturing stage. HAZ and Fusion Zones are larger in TIG compared to laser ones.

Metallurgical analyses have assessed two phenomena to smooth in their non benefit effects: too much hardening level in the fusion zone (brittle welds), and decreasing hardness level in HAZ compare to base material (creep troubles expected). Solutions developed in two important tasks in TTMS-004 field:

- PWHT process optimization,
- Eurofer filler wire chemical composition optimization are expected to apply their conclusions in next development stage of this joining development.

For TBM design aspects, this report shows clearly the necessity to modify the design of the Horizontal Stiffening Grid: the distance between the end face of Horizontal Stiffening Grid and the first cooling channel face must be at minimum for Laser process 5 mm and TIG process 7 mm. If not, first cooling channel will be distorted and too much stressed, over plastic limits.

REPORTS AND PUBLICATIONS

Final report : Micro structural analysis and qualification of joints and welds from TBM mock-up fabrication, Task TW5-TTMS-004-D02, Ph. Aubert, Report DTH/2006/98, December 2006.

TASK LEADER

Guillaume de DINECHIN

DEN/DM2S/SEMT/LTA
CEA-Saclay
F-91191 Gif-sur-Yvette Cedex

Tel. : 33 1 69 08 17 67
Fax : 33 1 69 08 90 23

e-mail : guillaume.dedinechin@cea.fr

**Task Title: QUALIFICATION FABRICATION PROCESSES
CHARACTERIZATION OF WELDING DISTORSION
OF SIMPLIFIED WELDED MOCK-UPS**

INTRODUCTION

This work is part of developments aiming to process high quality welds according to Helium-Cooled Lithium-Lead (HCLL) DEMO Blanket Module design. Several parts of the test blanket module are planned to be joined by welding process. This task follows the development of task TW2-TTMS-004-D02 and is in close link with the task TW2-TTBC-002-D02 (mock-up fabrication by CEA) and TW5-TTMS-004-D03 (residual stress characterization by ENEA). The main task objective is to produce simplified mock-up of the TBM's stiffening grid assembly in order to characterize the residual stress and the distortion induced by the welding process. The experimental trials will be compared to numerical simulations carried out with the finite element code SYSWELD®.

2006 ACTIVITIES

To improve the weldability of Eurofer TW2-TTMS-004-D02, it was decided to use the laser dual beam process. This new process improves the thermal field uniformness and limits the hot cracking risk during the welding operation. In order to perform a good welding simulation the most important fact is to model precisely the heat input of the welding process.

Heat source identification of the laser dual beam process

The laser dual beam process consists in two spots focalized on the top surface of the part between the weld line (figure 1).

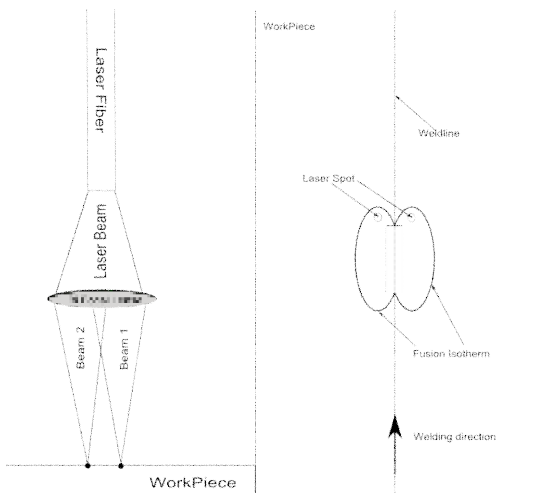


Figure 1: Basic principle of the laser dual beam process

The laser power input is modeled according to the Cylindrical-Involution-Normal (CIN) formula. This heat source allows to model a lot of welding processes. The CIN's energy distribution is given by:

$$q(x, y, z, t) = \frac{k \cdot K \cdot Q}{\pi \cdot (1 - e^{-K \cdot s})} \cdot e^{-k \cdot (x^2 + y^2)} \cdot e^{-K \cdot z} \cdot (1 - H(z - s))$$

- Q power (J)
- t time (s)
- k heat source concentration (mm⁻²)
- K involution factor of heat source (mm⁻¹)
- s heat source penetration depth (mm)
- $H(z - s)$ Heaviside's function
- x, y, z coordinate system (mm)
- q heat source power input in volume (J.mm⁻³)

Two weldments, with the same welding process conditions, are carried out at the French Laser Center GIP/GERAILP, with a YAG laser of peak power of 4 kW. One is an instrumented welding trial dedicated to heat source identification for Finite Element Analysis, the other is realized for further residual stress measurement by neutron diffraction.



Figure 2: Instrumented welding trial for the laser dual beam heat source identification

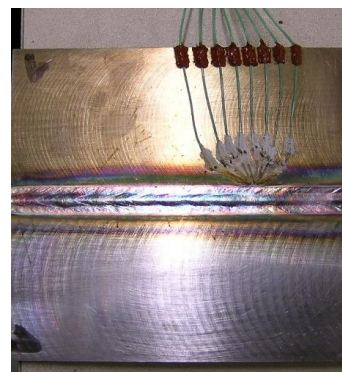


Figure 3: Thermocouples position after the welding operation

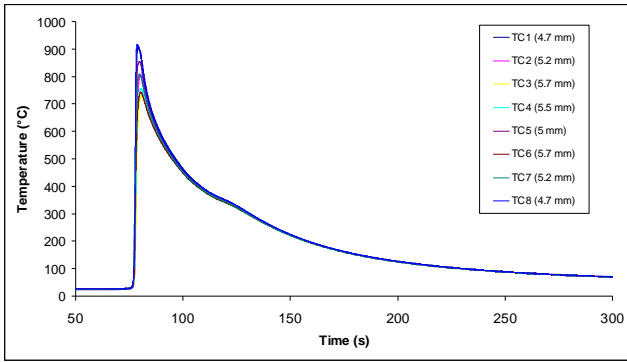


Figure 4: Temperature measured by the thermocouples

Preliminary calculation of residual stress on a T shape mock-up

In this study the joint is realized in 2 passes, one at the upper side and the other at the bottom side. Two modes are considered: Mode I, consists in, successive and opposite direction of the passes; Mode II, consists in, simultaneous and same direction of the passes (figure 5).

The simulation are performed with the finite element code SYSWELD™, the thermo metallurgical model for Eurofer is used [2], Thermal field and heat affected zone simulation in joining horizontal plate to vertical plate is presented in figure 6.

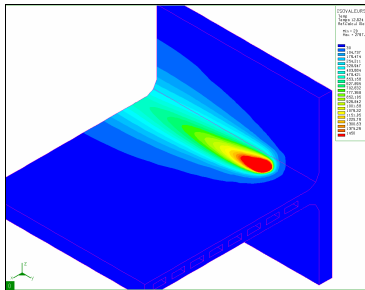


Figure 6: Temperature field during welding of the first pass

The equivalent Von Mises residual stresses are located in the HAZ and are similar for both modes. The level is high (> 850 MPa) due to the high yield stress of freshly formed martensite (figure 7 and figure 8).

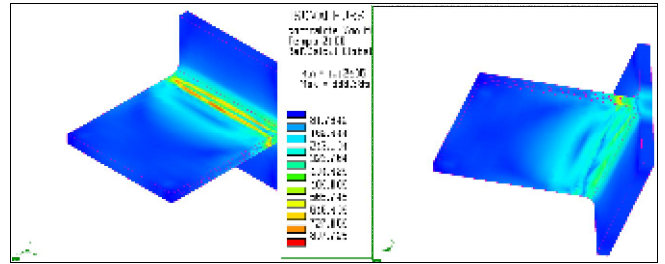


Figure 7: Equivalent Von Mises residual stresses Mode I Top & Bottom View

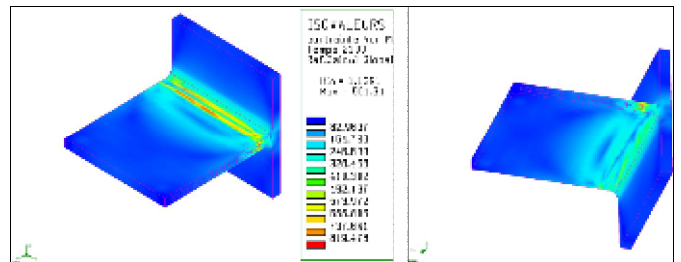


Figure 8: Equivalent Von Mises residual stresses Mode II Top & Bottom View

Neutron diffraction measurements of residual stress field will be carried out at the High Flux Reactor of the ILL-Grenoble in the frame of TW5-TTMS-004-D03 by ENEA. This preliminary calculation on a T-shape mock-up is used to determine the most relevant areas to investigate in the welded sample.

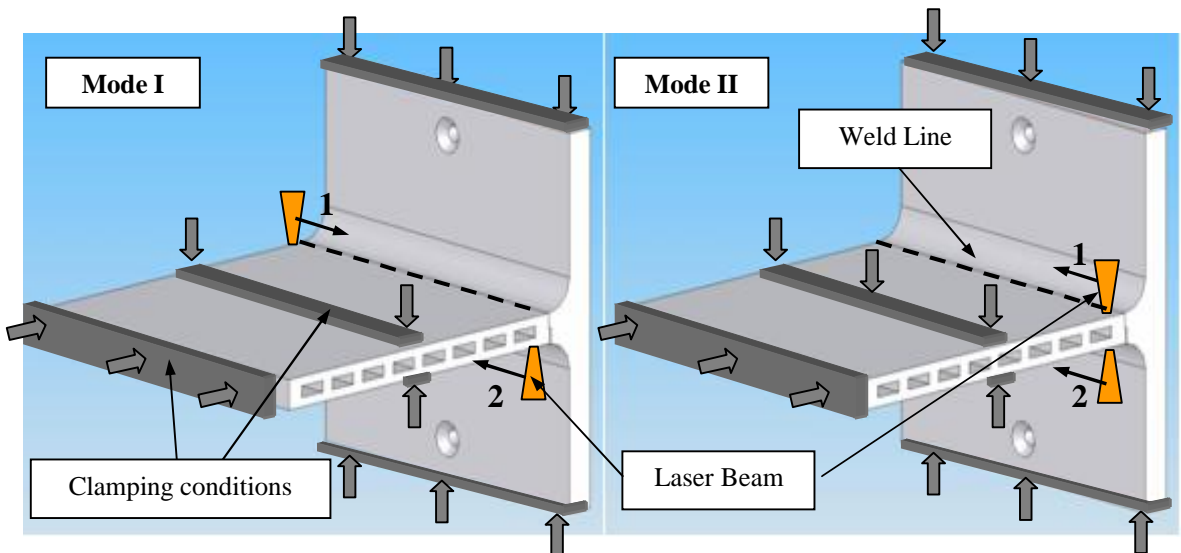


Figure 5: Assembly Mode I and II and clamping conditions

REPORTS AND PUBLICATIONS

- [1] O. ASSERIN “Intermediate report: Representative TBM welded mock-up: simulation of the welding distortions”

- [2] O. ASSERIN, “Processing of high quality welds according to TBM design”
CEA/DRT/DECS/UTA/03-RT37

TASK LEADER

Olivier ASSERIN

DEN/DM2S/SEMT/LTA
CEA-Saclay
F-91191 Gif-sur-Yvette Cedex

Tel. : 33 1 69 08 16 87
Fax : 33 1 69 08 90 23

e-mail : olivier.asserin@cea.fr

**Task Title: QUALIFICATION FABRICATION PROCESSES
WELDABILITY OF DISSIMILAR TUBES (EUROFER/SS316L)
BY FUSION BUTT WELDING WITH YAG LASER**

INTRODUCTION

The aim of that task is to characterize dissimilar EUROFER/SS316L laser butt welded joints, which is the configuration required for the Tritium Blanket Module external branch pipes. The LiPb tube internal diameter is 87 mm in wall thickness 6 mm and the He tube internal diameter is 60 mm (He input) and 70 mm (He output) in wall thickness 5 mm. To perform this task, we have followed the following route:

- CAD assessment of the laser welding tools required to weld the TBM external branch pipes;
- Laser butt welding tests of tubes (EUROFER, SS316L, EUROFER to SS316L) to assess the weldability, the overheating effect and the welding position effect.

Metallographic and non destructive/destructive characterisation of the dissimilar EUROFER/SS316L welds performed.

2006 ACTIVITIES

CAD characterization of YAG laser tools required for TBM's branch pipes welding configuration

In figure 1 is presented the actual version of the Helium Cooled Lithium Lead (HCLL) breeding blanket (TBM).

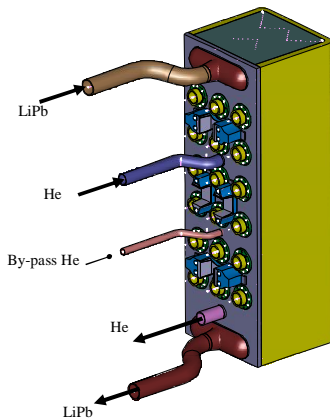


Figure 1: branch pipes of the HCLL breeding blanket

The TBM consists in a portion of the generic HCLL-DEMO blanket module adapted to fit the ITER test port.

The TBM features a steel box of 1832 (poloidal) × 585 (radial) × 626 (toroidal) mm³ overall dimensions, formed by an U-shaped First Wall / Side Walls (FW/SW). The box

is cooled by He circulating in toroidal/radial/toroidal channels and closed by two cooled caps (upper and bottom). It is closed, in the rear, by a Back Plate (BP) acting also as He collector and distribution system.

The BP collector region is made up of two thick outer plates (30 and 40 mm thick) having structural functions and two intermediate thinner plates (8 mm thick) for the He flow separation. The inner plate contributes to guarantee the integrity of the module box in case of internal pressurisation (in faulted conditions). Stiffening beams are foreseen between the 1st and the 4th back plate to make the collector able to resist to the internal He pressure (8 MPa in operating conditions). All plates are drilled to allow the crossing of the feeding/manifolding pipes and of the stiffening plates as well.

The TBM is made in EUROFER material and connected to the 316 L structural and external chamber. The EUROFER inlet/outlet He and LiPb tubes are then welded to 316LN tubes in the same diameters and wall thicknesses.

The actual dimensions of the LiPb inlet/outlet EUROFER tubes are a diameter of 87 mm in wall thickness 6 mm; the He inlet tube dimension is 60 mm with a wall thickness 5 mm and the He outlet tube dimension 70 mm with a wall thickness 6 mm. The minimal distance between two tubes is 156 mm.

Due to the geometry and practical considerations, welding is easier to perform with the YAG laser technology instead of the CO₂ laser technology. The YAG laser beam is delivered through an optical fibre to the welding head, where it is collimated then focused on the working area. The possibility to bring the YAG laser power through an optical fibre allows flexibility to the geometry to weld. In figure 2 is presented standard commercial welding heads.

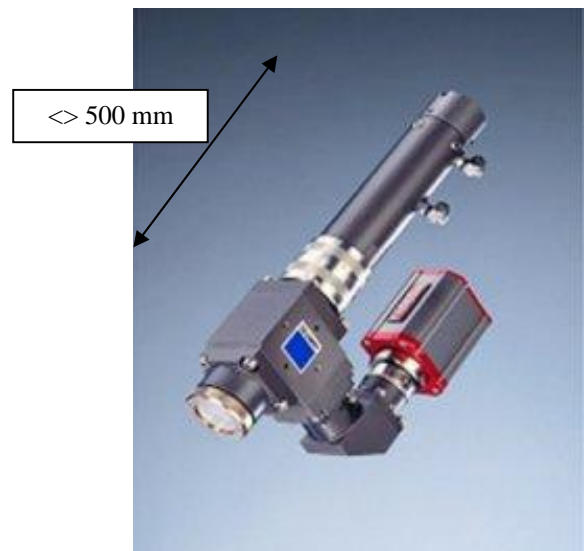


Figure 2: Example of standard commercial welding head

The easier way to perform the dissimilar EUROFER/316LN welds would be to use a standard welding head turning around the tubes to weld. Unfortunately, in reason of the dimensions of these heads and the minimal distance between the branch pipes (actual design), it seems not possible to apply this welding procedure with standard cw-YAG laser tools. In addition to these considerations, the laser suppliers don't sell on the shelves YAG laser installations able to move a laser welding head around a fixed tube.

An other way would be to weld from inside the tubes. A specific welding head is inserted inside the tubes and aligned on the joint. Such specific heads as the one shown in figure 3 must be developed for these specific welding configurations. The beam is delivered through an optical fibre to the welding head, where it is collimated, reflected into a cooled mirror, and focused on the working area. Specific tool optimisations must be performed on that kind of tools to be sure to be able to bring the YAG laser inside small diameter tubes. Such specific studies were developed in the GIP GERALIP French laser centre for ITER needs. These welding heads are available for a laser power of 2 kW maximum; nevertheless, more developments are needed to achieve such specific industrialized laser welding tools.

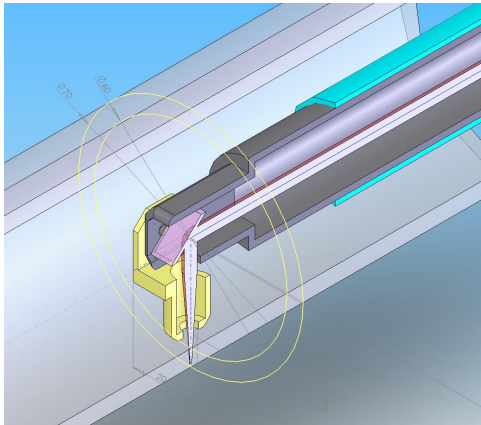


Figure 3: Specific welding heads in development

EUROFER/316L WELDS

Two kinds of steel grades are procured for that welding study: an EUROFER tube in external diameter 56.6 mm and in wall thickness 3 mm (appendix 1) and a 316L steel in external diameter 60.3 mm and in wall thickness 5.5 mm (appendix 2). The austenitic steel tube is machined to get a tube of diameter 57 mm and in wall thickness 3mm. The tubes are cut in 100 mm long samples, for the welding tests.

Remark: Eurofer tubes were not available in the wall thickness 5 mm (wall thickness of TBM external branch pipes). Nevertheless, as with the wall thickness 3 mm, 5 mm laser butt welds are achievable in wall thickness 5 mm without a groove and without a filler wire.

For the welding tests, it is used the following installation:

- A continuous ND-YAG laser HL4006D.
- A standard welding head with a 200 mm collimating lens, a 150 mm focusing lens and a reflecting mirror between the two lenses.

The tubes are fixed into a rotating clamp. For these welding tests, the welding head is fixed and the tubes are brought into rotation (figure 4).

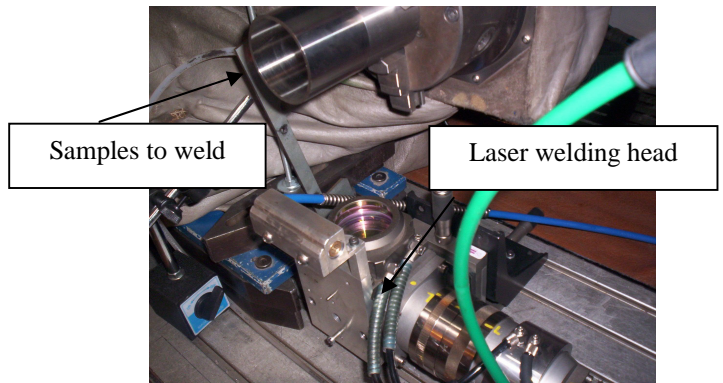


Figure 4: Welding installation

Argon is used inside and outside the tubes to protect the welding pool. Before performing the weld, 5 to 6 tacking welds of length 1.5 mm are made on the joint around the tube. The laser power increasing slope is 150 ms and decreasing slope 100ms. The laser beam is focused 0.2 mm inside the tube.

The welds are performed with different welding positions: it is studied whether the welding position has an influence on the melted zone geometry and whether, with tubes of that diameter and that thickness, we observe an overheating effect near the seam overlapping.

Dissimilar butt welds on tubes without a groove were already performed with the EB and TIG processes, but in wall thickness 1.5 mm and 2 mm. It isn't possible to use the TIG process to achieve welds in one pass for butt welds in thickness up to 2 - 3 mm above that thickness, it is necessary to machine a groove and to fill it with a filler wire. With the EB and laser fusion welding processes, butt welds in one pass and without filler wire are achievable in thickness up to 3 mm. In particular, TBM branch pipes in thickness 5 and 6 mm are weldable in one pass and it is much easier to use the laser process than the EB process.

In figure 5 is presented a good looking dissimilar laser butt weld.

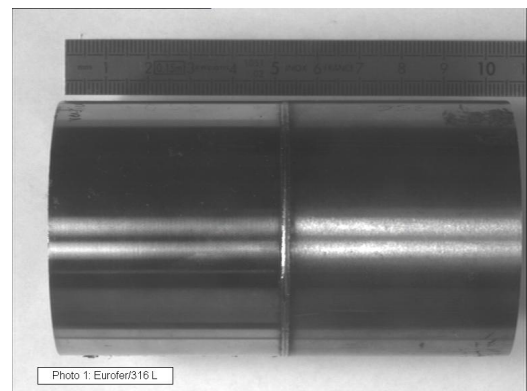


Figure 5: Example of a dissimilar laser butt weld

The cuts don't reveal any overheating effect during welding between 0° and 180° (the fact that, during welding, and on the same weld, the size of the welding pool increases due to "overheating" effects). It seems to be a light welding position effect on the melted zone width inside the tubes (figure 6).

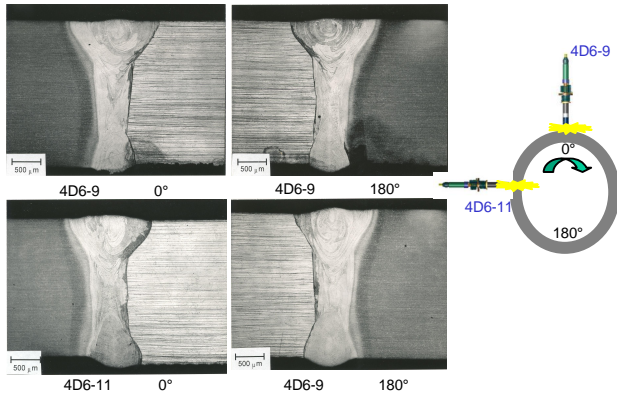


Figure 6: Metallographic cuts in the dissimilar EUROFER/316L laser butt welds

Non destructive and destructive characterization

In applying the quality criteria from the RCCM construction code, the X rays control is declared conform. The entire weld is controlled. For each weld, two shoots are performed.

In the transversal traction tests at room temperature, all the welds break in the austenitic tube: in the base material, 1.5 to 2 cm away from the weld (figure 7). The load for breaking is around 14 kN (577 to 611 MPa). The specimens are machined in the tubes: to perform the test, each extremity of each specimen is flattened in order to be inserted in the traction machine.

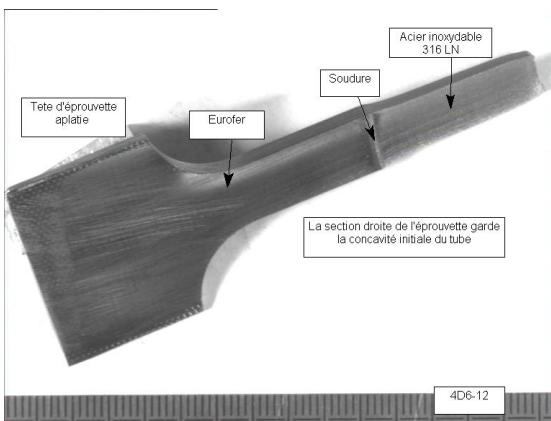


Figure 7: Example of a broken specimen during the traction test

CONCLUSIONS

The aim of that task is to characterize dissimilar laser welding joints of TBM tubes in butt joint design. Eurofer/316L welds are performed on tubes in wall thickness 3 mm. Sound welds are processed.

The characterization of these welds brings the following results:

- There is no overheating effect between 0 and 180°;
- The size of the welding zone depends slightly on the welding position (specially inside the tube) and sound welds are obtained in the welding positions 0°, 90°, 180° and 360°;
- The tensile strength of the welds is superior to the strength of the austenitic tube.

So, the laser process is able to achieve welds in wall thickness 3 mm meeting the usual requirements. It should be the same with tubes having the same wall thickness of the external branch pipes, 5 to 6 mm. As with 3 mm, the laser process doesn't need to machine a groove and to use a filler wire to weld tubes in wall thickness 5 or 6 mm (when there is no gap between the tubes to weld). To bring that demonstration, it would be necessary to attend the following way : procurement of EUROFER tubes in the right wall thickness, development of a welding installation to weld the tubes in turning around the tubes (strategy 1), development of a welding installation to weld from inside the tubes (strategy 2), perform the welds and their characterization. These welding installations should take into account the necessary laser power to weld in wall thickness 5 or 6 mm (superior to 2 kW, as it is shown in that study for the wall thickness 3 mm).

REPORTS AND PUBLICATIONS

- [1] DTH/DL/2006/80 Weldability of dissimilar tubes (EUROFER/SS316L) by fusion butt welding with YAG laser – G. de DINECHIN, O. BLANCHOT

TASK LEADER

Guillaume de DINECHIN

DEN/DM2S/SEMT/LTA
CEA-Saclay
F-91191 Gif-sur-Yvette Cedex

Tel : 33 1 69 08 19 57
Fax : 33 1 69 08 90 23

e-mail : guillaume.dedinechin@cea.fr

TW5-TTMS-004-D07

Task Title: QUALIFICATION FABRICATION PROCESSES WELDABILITY OF EUROFER HOMOGENEOUS PLATES

INTRODUCTION

Eurofer weldability must be assessed for the Tritium Blanket Module (TBM) development and manufacturing. TW5-TTMS-004-D07 task is dedicated to characterize Eurofer joints on flat samples for feeding the developments for the realization and manufacturing feasibility demonstration mock-up, performed in TW2-TTBC-002-D02 task. The aim of this subtask is to assess the feasibility of Eurofer welding, with the required welding processes for TBM manufacturing in welding situations, close to real joint design.

2006 ACTIVITIES

The TBM modules require a large number of Eurofer welds for a complex structure. The weldability must be assessed on real joint configurations on the second batch of Eurofer. Electron beams, Hybrid (MIG/Laser), TIG and laser welding processes have been applied on flat samples. Welding operating conditions are optimised in the stationary stage to process sound joints. Welding configurations are divided in two sketches, as following:

- Electron Beam and Hybrid: thickness 25 to 40 mm,
- YAG Laser and TIG: 8 mm (4 mm on both sides).

Welding requirements are sound structural welds, free of cracks with high joint coefficient and low pores level. Mechanical weld performances of this report will feed TBM code work for RCCMR codes requirements.

HYBRID WELDING

TBM Cap thickness is today fixed to 32 mm. CEA promotes, in the purpose of distortion reducing, MIG/laser hybrid process, developed since several years for ITER. For the following welding trials on 25 mm thickness plates, a Eurofer standard filler wire, 1 mm diameter, has been used for hybrid joining tests. Hybrid process is a high speed multi-pass welding process procuring a travel speed in the range of 1.3 m/min, compared to the reference one Narrow Gap TIG welding (travel speed in the range of 0.1 m/min), with a quite reduced groove width (figure 1): 8 mm at the groove top, compared to 14 mm for Narrow Gap TIG process (NGTIG). Each welding pass performs 2.5 mm penetration depth thickness, to compare with 1.2 to 1.5 mm in NGTIG. Deposited mass is ten times higher in hybrid process, and distortions are obviously reduced. Hybrid process consists in combining Nd:YAG continuous laser and MIG processes. The two processes interact in the same molten pool. In first approximation, laser and MIG welding energy are roughly in the same level, around 4 kW.

For getting an enough sidewall welding penetration on the chamfer groove, the laser beam is divided into two spots, which bring thus more welding energy close to chamfer walls. Side wall penetration thickness in the range of 1 mm is thus obtained. High depth Eurofer hybrid welding has been operated on 400 x 300 x 20 mm³ samples with no waiting time and no joint cleaning between each filling pass on a Kuka KR30HA robot in two ways:

- Standard multi pass welding (14 passes),
- Multi passes welding with pre-(200°C) and post-heating during 2 hours at 300°C (14 passes).

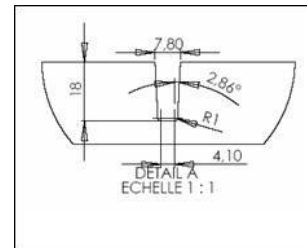


Figure 1: Narrow Gap Hybrid joint design

The welds obtained for each welding pass have good external aspect without oxidation, as shown on figure 2. Shiny surfaces of the welded plates show a low level of heat loading during welding.



Figure 2: External view of Hybrid weld

Metallurgical aspects

On each welded joint, transverse cross sections have been achieved (figure 3).

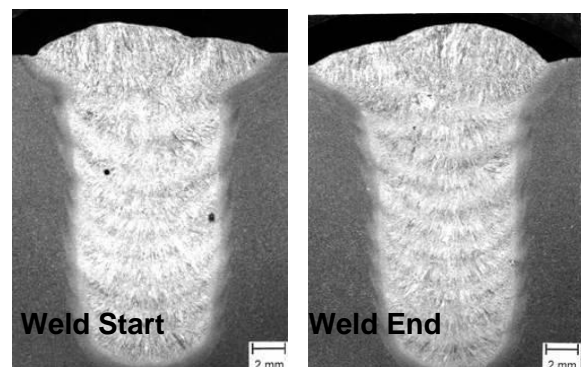
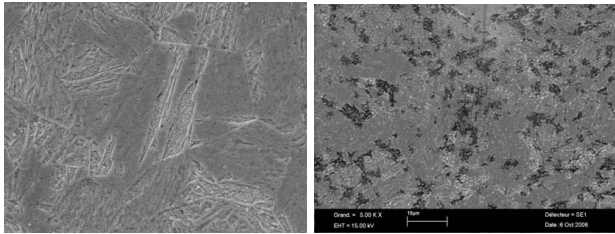


Figure 3: Hybrid transverse macrographs

Hybrid welds look homogeneous and its borderlines quite nearly parallel. It is observed no defect such sticking, and only few pores (0.3 mm diameter). It shows good weld geometry and the side wall penetration depth measured is in the range of 0.5 to 1 mm, which is in the same range than the reference NGTIG process.

Hybrid welds show coarse grain formation in the fusion zone. Equiaxed grains with 20 µm grain size of martensite laths are fully produced in all welds, which is twice the base material grain size (12 µm). No δ ferrite and carbides have been observed in the fusion zone. This illustrates the “relative” low level of cooling rate during welding solidification, compared to Electron Beam and Laser cooling rates. Micrographs cross sections are presented in figure 4.



Fusion zone microstructure HAZ microstructure
Figure 4: Hybrid welds microstructure

No difference in the Fusion Zone between the two welding conditions with and without pre- and post-heating treatment is observed: same microstructure and grain size. Coarse grain zone can be observed in the zone where the layer of the former welding pass is affected by following one. No specific HAZ effect is observed in the multi-layers due to multi-pass welding process (hardness oscillations inside the Fusion Zone seen only on the hardness profile).

In Heat Affected zone (HAZ), the microstructure is on type fine martensite grains with fine M₂₃C₆ carbide precipitates which are small size white points on figure 4. Former “mother” austenite grains are more fine (8 µm) than those observed in base material. Compared to the base material the grain size is smaller in the HAZ by about a factor of 2. HAZ is driven by α → β transformation fully martensitic, with smaller grain size than in base material, and carbide coalescence. Ferritic-martensitic steels such Eurofer suffer from hardening and embrittlement, due to uncontrolled martensite formation in the vicinity of the HAZ. The grain coarsening in the weld is not so different and fine HAZ grained are visible even in the transition region at the top and middle layers.

Profile Hardness

Maximum hardness level is observed in the fusion zones. It varies between 410 and 490, explained by the multi-pass welding procedure. Each welding pass (1.5 to 2 mm penetration depth) induces a smoothing zone, considered as local HAZ. The influence of the 200°C pre- and post-heating is very low for reducing these hardness fluctuations. The hardness average level in fusion zone is too high for both welds and will reduce strongly weld ductility and fatigue behaviour. An average hardness level in the range of 300 - 350 HV is expected for TBM manufacturing.

The pre- and post-heating temperature of 200°C is not sufficient to minimize hardness variations inside the fusion zone and also the hardness difference (≈ 220 to 230 HV1) between fusion zone and base material.

HARDNESS PROFILE of 06P014-2 sample with post heating at 50% weld penetration depth

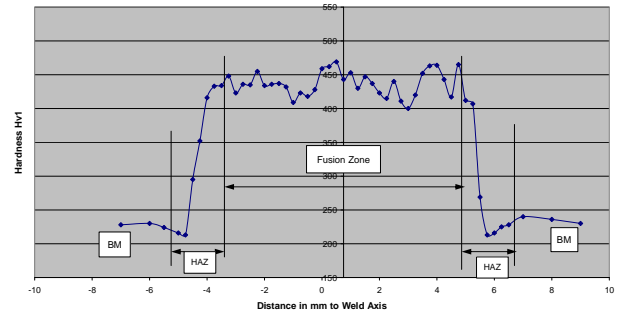


Figure 5: HV1 profile hardness

The benefit of the pre- and post-heating treatment to smooth these phenomena has been demonstrated through another project, with the same welding configuration, applied on 9% Chromium steel, (same steel family) with 400°C pre- and post-heating temperature. It has been seen a strong reduction of Fusion Zone hardness from 450 HV1 to an average level of 280 HV1, which seems to be acceptable. However, the smoothing effect in HAZ is still observed, which shows the necessity of a high temperature PWHT treatment, to restore good weld properties.

Mechanical tests

Some samples have been machined fully inside the fusion zone. They have the same axis than the weld. They are dedicated to determine the joint coefficient. Tensile tests have been performed at room temperature. Two situations have been tested (figure 6):

- Samples machined in joint with no PWHT,
- Samples with tempering PWHT: 750°C – 2 hours.

| 06P014-2 sample | No PWHT sample | 750°C – 2 hours PWHT sample | Base Material |
|---------------------------------|----------------|-----------------------------|---------------|
| Sample diameter (mm) | 4 | 4 | |
| Section (mm ²) | 12,5 | 12,7 | |
| 0,2% offset Yield Stress (MPa) | 850 | 835 | ≥ 400 |
| Ultimate Tensile Strength (MPa) | 1047 | 925 | 580 – 700 |
| Total Elongation (%) | 17 | 15 | ≥ 20 |
| Reduction Area (%) | 64 | 65 | |

Figure 6: Mechanical testing (samples along joint)

Due to the fact that weld strength is higher than base material, it can be considered that **HYBRID JOINT COEFFICIENT VALUE IS EQUAL TO 1**. However, total elongation is a little bit below of the base material value: 25 %.

Other tensile samples with axis in transverse direction to the weld have been machined (figure 7).

| 06P014-1 sample | With PWHT | Base Material |
|---------------------------------|-----------|---------------|
| Sample diameter (mm) | 10 | |
| Section (mm ²) | 79 | |
| 0,2% offset Yield Stress (MPa) | 556 | ≥ 400 |
| Ultimate Tensile Strength (MPa) | 681 | 580 – 700 |
| Total Elongation (%) | 22 | ≥ 20 |
| Reduction Area (%) | 78 | |

Figure 7: Mechanical testing (samples transverse joint)

All tested tensile samples have broken in base material, which is the minimum required. Weld performances are quite good: ductile welds with strength at higher level of base material performances.

ELECTRON BEAM WELDING

A second welding process is foreseen for Cap/First Wall: Electron Beam process (EB). In the Eurofer second batch, no 40 mm thickness sheets were available for performing welding trials. Low thickness of available Eurofer sheets (25 mm), impede to process tensile tests for this welding process. For this reason, CEA has asked to M. Rieth from FZK for shipping to CEA a 40 mm Eurofer sample EB. The following welding parameters have been applied: High voltage: 150 kV, Welding current: 72 mA, Travel speed: 0.3 m/min. CEA has conducted metallurgical characterization (figure 8) of this sample, in the same way than hybrid process.

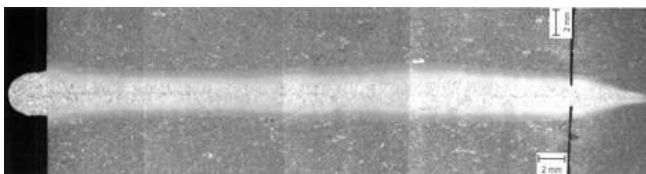


Figure 8: Macrograph cross section of EB weld

The thickness sample is 40 mm and weld width 2 mm. At the bottom of the 40 mm plate, a second plate, so called beam stopper, has been located to avoid undercuts, and drive root pass weld defects generally observed in EB process inside this second Eurofer plate. There is no defect inside the weld, free of cracks, bubbles and inclusions. Figure 9 shows the δ ferrite apparition, which is quite sensitive to magnetic effect.

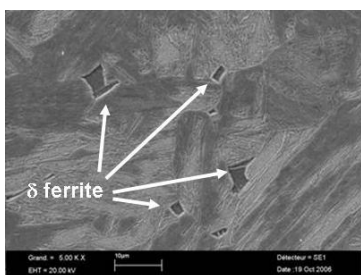


Figure 9: Fusion zone with delta ferrite

The δ ferrite indicates a too much high cooling rate, which explains coarse grain and high hardening level in the fusion zone. The grain size of EB weld fusion zone is small: 20 to 30 μ m, a little bit greater than Hybrid welds, due to the higher welding energy injected to produce a 40 mm

penetration depth, to compare with 2 mm in multi-pass Hybrid welds. Fusion zone exhibits a strongly disordered coarse grain weld zone. No defect is observed. The hardness profile of Electron Beam weld at mid penetration depth is given in figure 10.

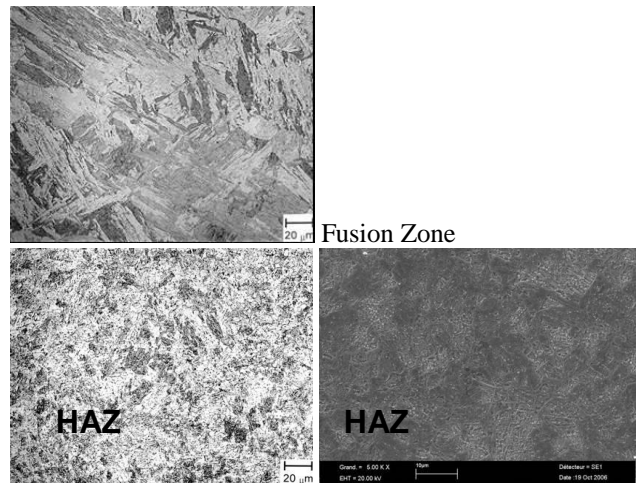


Figure 9: Micrograph cross section of EB weld

EUROFER 97 Electron Beam Welding PROFILE HARDNESS at half penetration depth

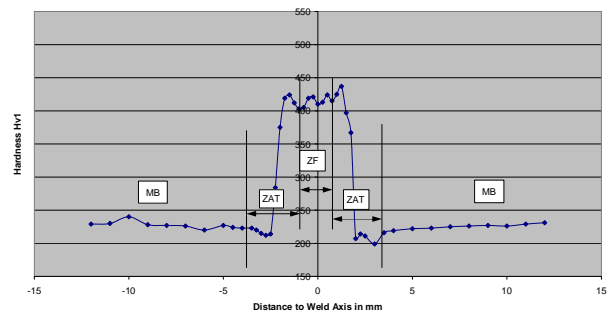


Figure 10: HVI profile hardness of EB weld

The only difference with hybrid welds is related in the very narrow width of fusion zone and HAZ, which will enhance metallurgical and mechanical troubles. The same level of hardness value of hybrid process is obtained in fusion zone and HAZ for EB process.

TIG WELDING

TIG welding experiments have been achieved on flat samples with a standard welding torch equipped with a 1.6 mm diameter tungsten electrode on flat samples. These welding tests have allowed developing TIG welding process, waiting for the specific low size torch providing, in TW2-TTBC-002-D02 task. The same coil of filler wire than Hybrid process experiments has been used. All welding developments have been carried out to minimize weld distortions, by reducing the weld penetration depth in the range of 1.5 mm for each welding pass, letting between each pass the work piece temperature decrease to room temperature inside the clamping device. After each weld, the sample has been extracted from clamping device, and then turned off, for processing the other side weld. The following welding sequence has been applied, by returning welded parts for each weld, as described in figure 11, with the following sequence:

- Root pass n°1 (side 1), root pass n°2 (side 2),
- Filling pass n°1 (side 1), filling pass n°2 (side 2),
- Capping pass (side 1), capping pass (side 2).

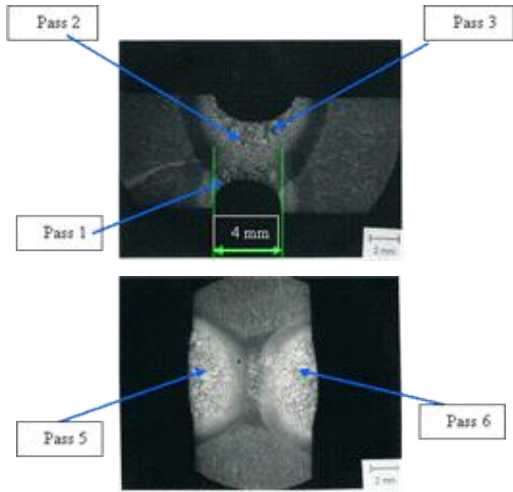


Figure 11: Multi-pass TIG welding sequence

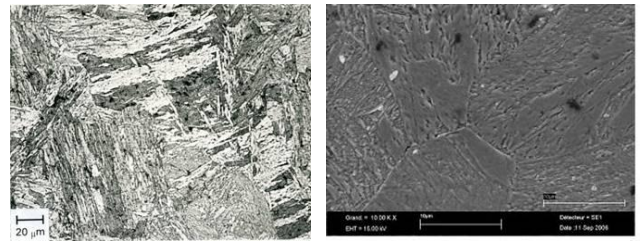
The process, even for a low thickness plate, can be classified in fact as a narrow gap TIG process with 6 welding passes. External faces of TIG welds are presented in figure 12, with quite smooth and shiny aspects. Sound welds are performed with reduced size welds compared to standard TIG welds. An average level of 0.26 mm pores diameter can be taken into account for TIG welds.



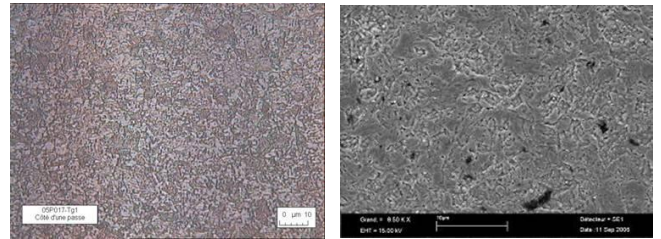
Figure 12: External faces of TIG welds

TIG welds microstructure

Metallurgical examinations have been carried out (figure 13). TIG welds show coarse grain formation in the fusion zone. Equiaxed grains of martensite laths are fully produced. No δ ferrite has been observed in the fusion zone. Grain size in fusion zone is quite irregular and in the range of 40 μm to 100 μm , which is twice to four times the base material grain size (20 μm). No defects like cracks and inclusions are observed in the welds. Compared to the base material, the grain size of the Heat Affected Zone (HAZ) is smaller by about a factor of two. In Heat Affected Zone (HAZ), microstructure is on type fine martensite with fine M_{23}C_6 carbide precipitates. Former “mother” austenite grains are more fine (8 μm) than those observed in base material. Formation of delta-ferrite could not be detected. The HAZ is driven by $\alpha \rightarrow \beta$ transformation fully martensitic, with smaller grain size than in base material, and carbide coalescence.



TIG Fusion Zone



TIG welds Heat Affected Zone

Figure 13: Multi-pass TIG weld microstructure

TIG hardness profile

Ferritic-martensitic steels, like Eurofer, suffer from hardening and embrittlement due to uncontrolled martensite formation in the weld and softening effect in Heat Affected Zone. Profile hardness curves are shown in figure 14. The average level for Fusion Zone is in the range of 436 HV_{0.5}, which is an increasing of 205 HV_{0.5} compared to the base material, and small decreasing in Heat Affected Zone. Hardness reducing effect in HAZ is related to carbide formation (fine M_{23}C_6 carbide precipitates). The hardness fluctuation in TIG Fusion Zone is explained by the multi-pass welding procedure, which produces layer by layer intermediate cooling phases.

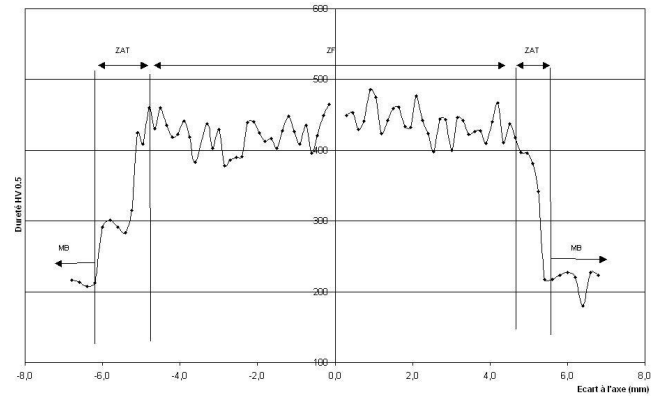


Figure 14: Hardness profile of flat samples TIG welds

Administrative troubles have driven some long delay in the purchasing of the compact low size 180 amps welding torch. So, real welds will be performed in 2007, in the frame of TW2-TTBC-002-D02 task, and will be mechanically tested.

LASER WELDING

Laser process induces less welding distortions than the other welding processes. Standard laser welding parameters have been applied on Eurofer samples, in performing a first 4.5 mm pass and a second 4.5 mm pass on the opposite side. YAG laser welding has started to define parametric process window. Work on laser beam shaping has been

conducted to get hemispheric weld shape for avoiding hot cracking effect. Thus cooling rate is automatically reduced and liquid motion inside the molten pool much smoother. Laser light is easily manageable by simply changing optics device. To obtain larger and low enhanced welds, laser energy distribution must be reduced and adapted to the material behaviour. Specific optics has been used to manage energy distribution profile, to adapt the heat source to laser weld shape to try getting hemispheric weld shape. Laser spot size of 300µm, 450µm, and 600µm have been tested, with distances between the two spots in the range of 600 µm to 4 mm. Laser beam de-focusing mode did not procure good results. The 4 kW available laser power is not sufficient to procure standard travel speed used in laser welding processing: above 1 m/min, in which the heat transfer is mainly assumed by convection mode. With a travel speed of 0.36 m/min, the molten pool formation is mainly driven by conduction mode, typical for arc processes. After a lot of welding experiments, following laser process parameters have been selected:

- Laser power: 4 kW,
- Travel speed: 0.35 m/min,
- Focal length: 150 mm,
- Twin spot with d = 2.1 mm,
- Laser beam focus on top surface work piece.

The available incident laser energy was too low to have a real laser welding process. CEA got in end November 2006 the most reliable and powerful one: Trudisk 8002 (disk laser, 8 kW) from TRUMPF in CEA/GERAILP plant in Arcueil. This laser will distribute, through a 200 µm optical fibre, a continuous laser power of 8 kW. It will be easier to manage laser process, by beam shaping the spot size, or waving at very speed the laser beam.

Metallographic characterization

On each welded joint, transverse cross sections have been made. Macrographs of nominal laser Eurofer welds are shown on figure 15.

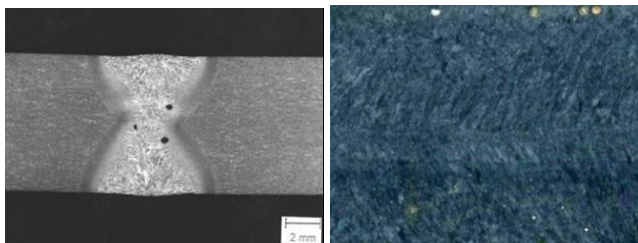


Figure 15: Transverse and longitudinal cross section

Fusion zone width is in the range of 5.8 mm for laser process in comparison to 7 mm for TIG process at top weld position. The laser passes are well interpenetrated, with no cracks. The two spots laser configuration has fully allowed eliminating the hot cracking phenomenon. Porosity is the major trouble for laser process. Hot cracking phenomenon has conducted to widen the molten pool, by twin spot configuration. In cross and transverse sections, it can be observed pore diameters from 0.08 mm to 1.2 mm for laser process with an average level of 0.32 mm, to be compared to 0.16 – 0.6 mm range with an average level of 0.26 mm for TIG process. Pores are localized at the bottom of each

weld pass, where the molten pool is not enough stable and quiet, in comparison with middle or top position. The solution to solve this problem is to use the new 8 kW laser with enhanced beam quality.

Laser weld microstructure

The grain size of laser weld Fusion Zone is small: 10 to 20 µm, in the same range than hybrid welds and rather smaller than TIG welds 40 µm to 100 µm and base material (20 µm). Fusion Zone exhibits a strongly coarse grain weld zone (figure 16). Equiaxe grains of martensite laths are fully produced. No δ ferrite has been observed in the fusion zone.

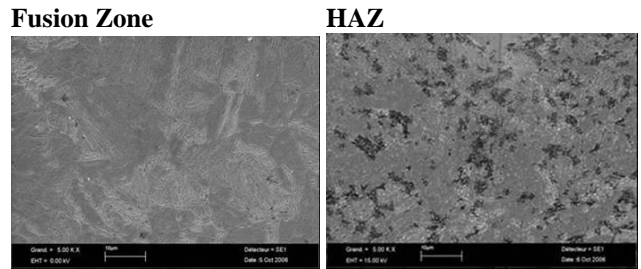


Figure 16: Laser welds microstructure

The Heat Affected Zone is composed of fine and decomposed martensite. The HAZ presents no delta-ferrite, fine grains smaller with a factor of 2 to 3, compared to fusion zone. HAZ width at 50 % welds penetration depth is in the range of 0.5 mm, which is quite low and 3 times smaller than TIG process. It indicates a very brittle joint. Small white points in high magnification rate of HAZ cross sections are carbide precipitation (fine M₂₃C₆ carbide precipitates), which will lead to a hardness reduction in HAZ, compared to base material. From these results, the necessity of Post Welding Heat Treatment seems to be analyzed, for reducing the coarse grain region of fusion zone, and carbides precipitation in the HAZ.

Profile Hardness

Profile hardness for laser mono spot welding is shown in figure 16. The hardness average level in laser Fusion Zone is very high: around 455 HV_{0,5} and 360 HV_{0,5} in HAZ.

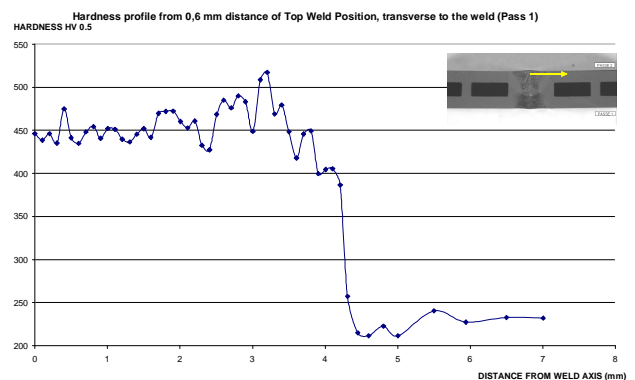


Figure 16: Laser weld hardness profile (Pass 1)

HAZ width is in the range of 0.5 mm, which is quite low and 3 to 6 times smaller than TIG process. The average level of hardness profile in Fusion Zone is quite the same for the two laser welding passes. The fluctuations are high

in this coarse and brittle area. It has been explained in hybrid welds tests in the former lines that a high temperature pre- and post-heating treatment (around 400°C – 450°C) during laser welding can:

- Reduce strongly hardness level in Fusion Zone,
- Decrease hardness fluctuations in Fusion Zone.

However, this heat treatment will complicate strongly the laser welding procedure and clamping device conception. The HAZ presents fine and decomposed martensite, no delta-ferrite, fine grains smaller with a factor of 2 to 3, compared to fusion zone. HAZ width at 50 % welds penetration depth is in the range of 0.5 mm, which is quite low and 3 times smaller than TIG process. It indicates a very brittle joint. Small white points in high magnification rate of HAZ cross sections are carbide precipitation (fine $M_{23}C_6$ carbide precipitates), which will lead to a hardness reduction in HAZ, compared to base material. From these results, the necessity of Post Welding Heat Treatment seems to be analyzed, for reducing the coarse grain region of fusion zone, and carbides precipitation in the HAZ. Laser welded samples have followed a tempering treatment, after welding phase, under the normalized conditions: 750°C during 2 hours (figure 17).

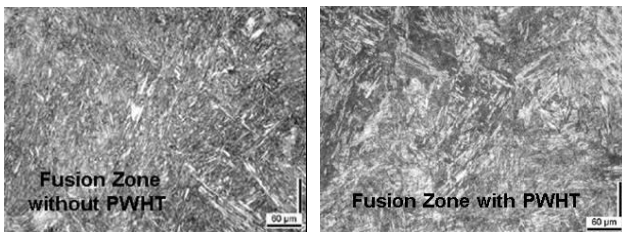


Figure 17: Fusion Zone with and without tempering PWHT

Between the two metallurgical states, no major difference is observed in microstructures and grain size: bainitic structure in Fusion Zone and bainitic + ferrite structure in Base Material. In Heat Affected Zone, fine $M_{23}C_6$ carbide precipitates are always observed with the tempering PWHT applied. Differences between the two metallurgical states will be only visible on mechanical performances.

Tensile tests

A comparison can be established on the two metallurgical states. Welding samples have been provided from 8 mm thickness plates from the second Eurofer batch, with Böhler Thyssen reference 993394.

Base Material with PWHT:

UTS = 663 MPa YS = 597 MPa TE = 34 %

Laser welds transverse tensile tests with PWHT:

UTS= 680 MPa Rupture in Base Material

Base Material without PWHT:

UTS = 1110 MPa YS = 830 MPa TE = 9 %

Laser welds transverse tensile tests without PWHT:

UTS = 710 MPa Rupture in Base Material

Reference Base Material without PWHT:

UTS = 580-700 MPa YS > 400 Mpa TE > 20 %

Compared to Eurofer reference base material, mechanical performances are in the scope of Eurofer reference, excepted Total Elongation value which is a little bit low.

This shows a stress level in the base material, before welding phase. Very high strength values are observed, and let think to an insufficient austenitising treatment, which affects obviously the ductility level, as observed in the performed tests. The consequence will be lower ductile-brittle transition temperatures (DBTT) in the impact test. After the tempering PWHT, reference values have been restored. The other performed tensile values show that, for all transverse tensile tests, the rupture occurs outside weld, in base material. So, LASER JOINT COEFFICIENT VALUE IS EQUAL TO 1.

A benefit effect of tempered PWHT is observed in the former results. More ductile welds are thus produced. A small reducing of UTS value with tempering PWHT samples will produce less brittle joints, which is demonstrated through the hardness profiles. With no PWHT, the same behaviour than the Hybrid welding samples is observed: too high hardening level in fusion zone, and reducing of total elongation level. With tempering PWHT, a high reducing rate of hardness profile has been reached. Hardness level in fusion zone is lower than 300 HV10, which was the initial objective. By comparison, with no PWHT, fusion zones present an average level of 440 HV1, comparable to all the former results. TEMPERING PWHT (750°C – 2 HOURS) IS EFFICIENT FOR FUSION ZONE HARDNESS SMOOTHING. Thus less brittle joints will be produced.

CONCLUSIONS

Metallurgical settings:

| WELD DEPTH (MM) | PROCESS | GRAIN SIZE (µM) | | Δ FER. | PORES (MM) | FUSION ZONE WIDTH (MM) | HAZ WIDTH (MM) |
|-----------------|---------|-----------------|-------|--------|------------|------------------------|----------------|
| | | FUS. ZONE | HAZ | | | | |
| BASE MAT. | / | 12-15 | 12-15 | NO | 0 | NO | NO |
| 40 | EB | 30 | 15-20 | YES | 0,3 | 3 | 1,5-2 |
| 20 | HYBRID | 20 | 8 | NO | 0,3 | 9 | 1,5-2 |
| 8 | TIG | 40-100 | 8 | NO | 0,26 | 7.6 | 2-3 |
| 8 | LASER | 10-20 | 10-15 | NO | 0,32 | 6.8 | 0.8 |

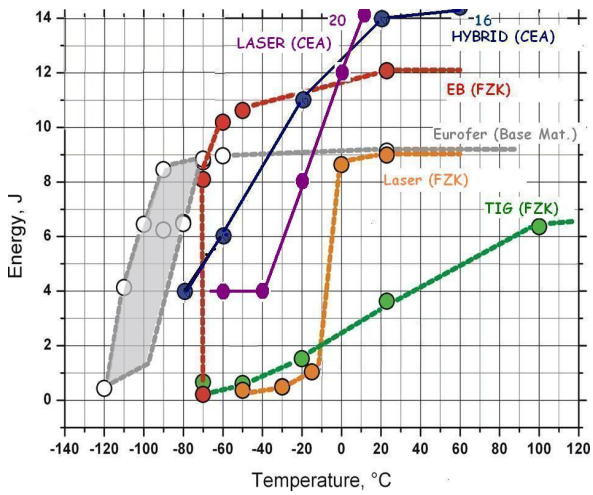
Tensile tests:

| PWHT processed: 750°C – 2 hours | Laser welds | Hybrid welds | Base Material |
|---------------------------------|-------------|--------------|---------------|
| Sample diameter (mm) | 4 | 4 | |
| Section (mm2) | 12,5 | 12,7 | |
| 0,2% offset Yield Stress (MPa) | 600 | 835 | ≥ 400 |
| Ultimate Tensile Strength (MPa) | 680 | 925 | 580 – 700 |
| Total Elongation (%) | 6,3 | 15 | ≥ 20 |
| Reduction Area (%) | 34 | 65 | |

For laser and Hybrid, joint coefficient is equal to 1.

TASK LEADER

➤ Impact tests:



PWHT must be processed.

Selected processes: Hybrid and laser.

REPORTS AND PUBLICATIONS

Final report: Eurofer weldability of homogeneous plates,
Ph. Aubert, technical report DTH/2006/99, December 2006

Philippe AUBERT

DEN/DM2S/DIR
CEA-Saclay
F-91191 Gif-sur-Yvette Cedex

Tel. : 33 1 69 08 37 99
Mobile : 33 6 08 53 36 41
Fax : 33 1 69 08 66 42

e-mail : philippe.aubert@cea.fr

**Task Title: HIGH PERFORMANCE STEELS
IMPROVEMENT OF FABRICATION PROCESS FOR
ODS-EUROFER: REFINEMENT OF CHEMICAL COMPOSITION
AND THERMOMECHANICAL TREATMENTS WITH EMPHASIS
ON THE FABRICATION ISSUES OF LARGER BATCHES**

INTRODUCTION

Compared to HIP, hot-extrusion process presents the advantage to induce a more homogeneous and finer microstructure without porosity, favourable features to optimise the material's performance and in particular to decrease DBTT values.

The main objectives of this task are to assess the process of hot-extrusion to obtain ODS-EUROFER with improved DBTT and to compare the effect of the yttria content (0.3 and 0.5%) on the tensile and impact properties of hot-extruded ODS-EUROFER alloys.

2006 ACTIVITIES

MATERIALS AND TESTS

The compaction by hot-extrusion was applied to mechanically alloyed powders of EUROFER with yttrium oxide contents of 0.3 and 0.5 wt % (supplied by FZK), which have been extruded at 1100°C as rod bars of 13mm in diameter and rectangular bars of 5mm thickness and 24mm width.

An homogenisation treatment at 1050°C for 15 min followed by a slow cooling has been applied to the rod bars. Rectangular bars have been cold rolled to 30% reduction in thickness then heat treated with the same conditions of time and temperature than the rod bars.

Tensile cylindrical specimens of 2mm in diameter and 12mm of gauge length and Charpy V-notch subsize specimens were machined in the longitudinal direction of the bars.

Tensile tests were conducted in the temperature range 20-750°C with a $7 \cdot 10^{-4} \text{ s}^{-1}$ strain rate.

Impact properties were obtained by Charpy tests performed over the range temperature -100 to +325°C to produce the full energy transition curve and the Ductile-Brittle Transition Temperature (DBTT) was evaluated by means of the hyperbolic tangent method.

IMPACT PROPERTIES OF MATERIALS CONSOLIDATED BY EXTRUSION AND HIP

To compare the impact properties of the ODS-Eurofer 0.3% Y_2O_3 consolidated by both methods, extrusion and HIP, the same homogenisation treatment (1050°C-15min) has been applied to a rod bar with 67mm in diameter consolidated by HIP at Plansee to obtain the same metallurgical condition.

Transition curves are presented in figure 1.

Extruded ODS-Eurofer 0.3% Y_2O_3 has a lower DBTT value (-40°C) and a higher USE (9J) than the hipped material (+70°C and 6J).

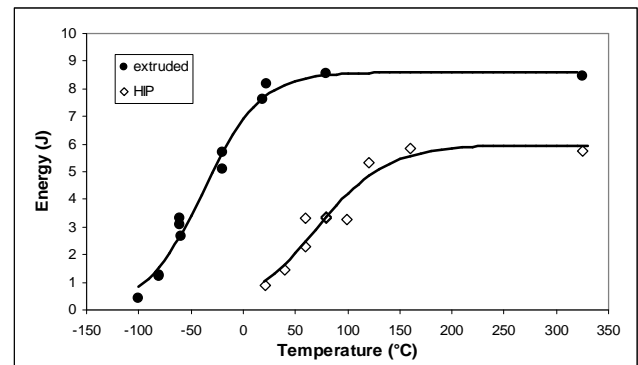


Figure 1: Effect of consolidation process (HIP and extrusion) on impact properties

EFFECT OF THE YTTRIA CONTENT

Transition curves of ODS-Eurofer 0.3% and 0.5% Y_2O_3 are compared in figure 2.

The yttria content does not affect the DBTT which remains about -40°C but the USE decreases slightly to reach the value of 6.5J.

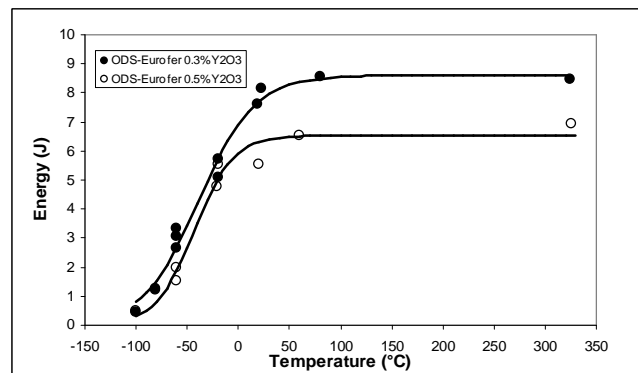


Figure 2: Effect of yttria content on impact properties

Tensile properties i.e the 0.2% Proof Stress, the UTS (Ultimate Tensile Strength), the total and uniform elongation were determined for each test temperature in the range 20-750°C.

The comparative evolution of the UTS as a function of the test temperature is reported on figure 3. For the two alloys, the evolution of the 0.2% P.S and the U.T.S with the test temperature is globally the same but values are a little bit

higher (about 50MPa for 0.2%P.S at room temperature) for ODS with 0.5% Y_2O_3 .

The gap decreases slightly with the increase of the test temperature. About ductility, the total elongation is around 20% for the two materials but a maximum of approximately 30% is observed at 550°C for ODS-Eurofer 0.5% Y_2O_3 .

Less specimens were available on ODS-Eurofer 0.3% Y_2O_3 and no tests were performed in the temperature range 325°C-650°C. The maximum of ductility around 550°C is perhaps present but has not been displayed.

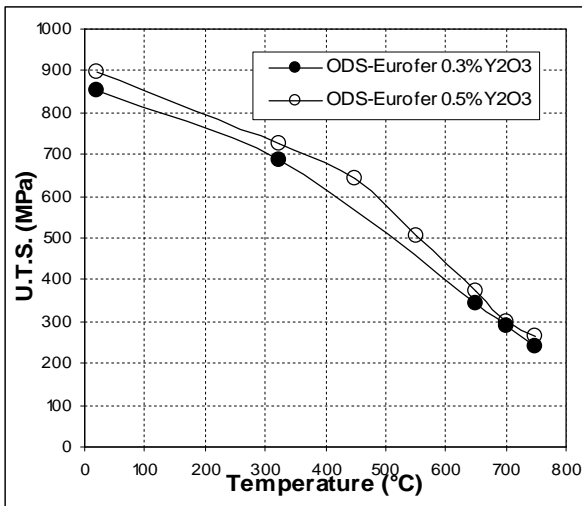


Figure 3: Effect of yttria content on the U.T.S

EFFECT OF THE PROCESS ON THE MECHANICAL PROPERTIES

After consolidation by hot-extrusion, the textures between the rod and the rectangular section materials are probably different. In addition, hot-extruded rectangular products are cold-rolled 30% in thickness before heat-treatment.

To evaluate the effect of the difference of process, impact and tensile tests in the longitudinal direction of the rod and the cold-worked plate were determined.

Transition curves for alloys with 0.3% Y_2O_3 are reported on figure 4.

The Ductile-Brittle Temperature (DBTT) of the as-extruded or as-extruded + 30% cold working are approximatively the same (-40°C) but a small decrease of the USE (6J) is observed for the cold rolled one.

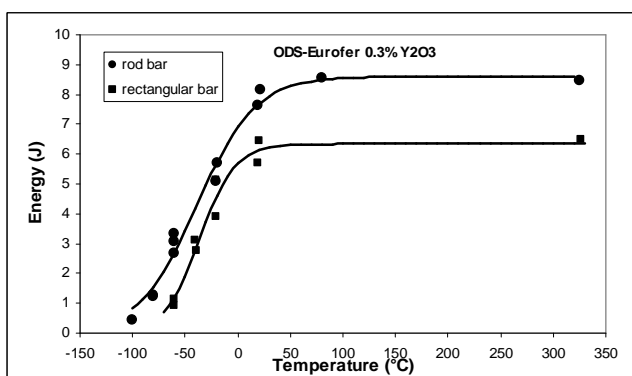


Figure 4: Effect of process (geometry and cold working) on impact properties

About tensile properties, the yield stress and the Ultimate Stress (figure 5) of the alloy are roughly the same for the two processes (hot extruded and hot extruded + 30% CW), we note only on the rectangular bar a little decrease of ductility except at 650°C (figure 6) where the maximum value of the total elongation is observed.

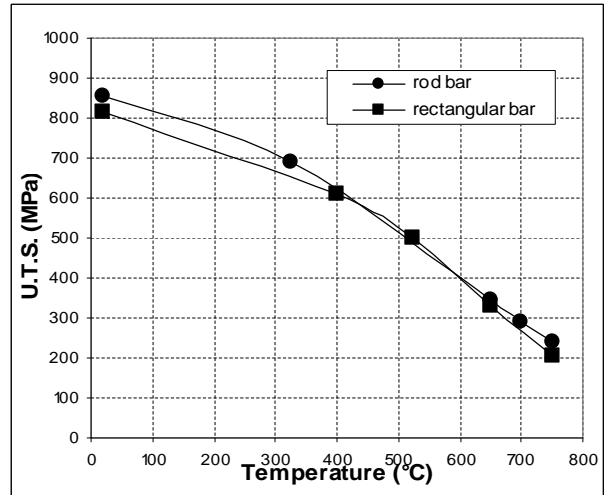


Figure 5: Effect of process (geometry and cold working) on the U.T.S

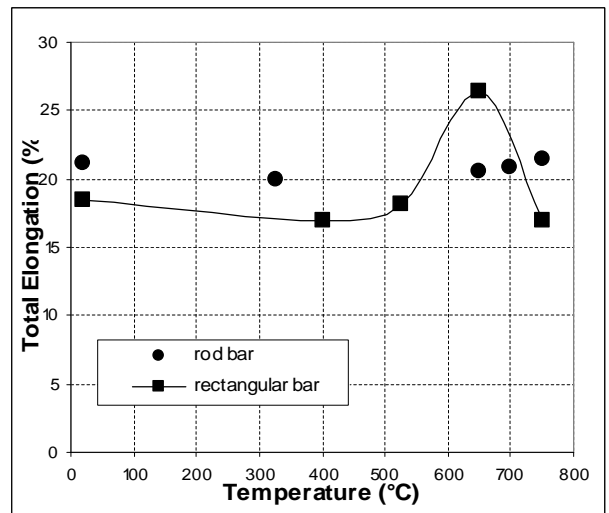


Figure 6: Effect of process (geometry and cold working) on the ductility

CONCLUSIONS

The mechanical properties of ODS-Eurofer alloys containing 0.3% Y_2O_3 and 0.5% Y_2O_3 have been characterised.

Results of impact tests performed on the ODS-Eurofer 0.3% Y_2O_3 consolidated by HIP at Plansee and hot-extruded at CEA confirm the interest of hot-extrusion to improve the strength and the DBTT of the material. The DBTT decreases from +70°C to -40°C and the USE increases from 6J to 9J.

The increase of yttria content from 0.3% at 0.5% has not a great effect on the mechanical properties. The DBTT is not modified and the USE decreases from 9J to 6.5J. Tensile strength is slightly higher (about 50MPa at RT) for ODS

with 0.5% Y_2O_3 and the ductility is around 20% for the two alloys.

Modifications on the process i.e the use of a die with rectangular section and a cold-working after hot-extrusion have no effect on the DBTT, it only decreases the USE from 9J to 6J.

Tensile properties are similar, only a slight decrease of ductility is detected.

REPORTS AND PUBLICATIONS

Final report: Mechanical characterisation of ODS-Eurofer bars produced by hot-extrusion, CEA report DMN/SRMA/LA2M/NT/2006-2786/A

TASK LEADER

Annick BOUGAULT

DEN/DMN/SRMA/LA2M
CEA-Saclay
F-91191 Gif-sur-Yvette Cedex

Tel. : 33 1 69 08 54 45

Fax : 33 1 69 08 71 30

e-mail : annick.bougault@cea.fr

Task Title: MODELLING OF IRRADIATION EFFECTS ON MICROSTRUCTURE EVOLUTION

INTRODUCTION

The experiments performed in the eighties by Takaki consisted in introducing point defects in the metallic matrix of pure iron by an electron irradiation at low temperature and in following the defect population kinetics by the technique of isochronal annealing of the electrical resistivity. In the absence of any experimental proof at the atomic level, the interpretation of these experimentally observed annealing stages have remained controversial for decades.

The long term evolution of the material is modelled with an event-based Monte-Carlo code (Jerk). The code rests primarily on the knowledge of the binding and migration energies of all the complexes which may form during the defect production itself and then during the annealing stages. A previous study conducted on pure alpha-iron [1] showed that the whole evolution could be quantitatively accounted for by a small number of basic parameters, which were computed through ab-initio techniques.

The aim of the present task was to extend to C-doped alpha-iron the work performed previously on pure iron. The present report shows that the approach used formerly can be successfully extended.

DETERMINATION OF BASIC INPUT PARAMETERS

The study relies heavily on a companion work of the EFDA programme which was in charge of calculating with the ab-initio code Siesta the binding and migration energies of complexes C_nV_m and C_nI_m where 'V' and 'I' stand for 'vacancy' and 'interstitial' respectively.

The complexes V_n and I_m had been determined in previously published studies [1]; their migration and binding energies are collected in tables 1 and 2. The capillary approximation consists in replacing the binding energy $E_b(n)$ of a n-cluster, when the latter is difficult to determine, by the value of the phenomenological law quoted below, which is known to hold well for large values of n and which is tuned to reproduce successfully the binding energy of a dimer:

$$E_b(n) = E_F + (E_b(2) - E_F) \frac{n^{2/3} - (n-1)^{2/3}}{2^{2/3} - 1}$$

where E_F is the formation energy of the single defect and $E_b(2)$ the binding energy of a dimer.

If the most stable configurations for I-C and V-C complexes can be determined without ambiguity, a thorough scan of all the possibilities for higher order clusters (I_2C , I_3C , V_2C , VC_2 , V_2C_2) was not made. The most

stable configurations were proposed on the basis of a trial and error procedure and reasonable binding energies can be proposed. It was found that the clusters could not migrate without dissociating partially or totally: as a consequence no migration energy for these clusters considered as a whole were proposed and only barriers for dissociation were evaluated.

Table 1: Migration energies (in eV) obtained with the ab-initio Siesta code for defect and defect-clusters and carbon interstitial atom

| $E_m(n)$ | n=1 | n=2 | n=3 | n=4 |
|--------------|------|------|------|------|
| Interstitial | 0.34 | 0.42 | 0.43 | |
| Vacancies | 0.67 | 0.63 | 0.35 | 0.48 |
| C atoms | 0.87 | | | |

Table 2: Total binding energies (in eV) obtained with the ab-initio Siesta code for defect and defect-clusters and carbon interstitial atoms in 3rd neighbour position. E_F stands for the defect formation energy of self-interstitial dumbbell and vacancy and for the energy of dissolution of one carbon atom into the lattice of iron.

| | n=2 | n=3 | n=4 | n=5 | E_F |
|------------|------|-------------------------|-------------------------|-------------------------|-------|
| $E_B(I_n)$ | 0.80 | capillary approximation | capillary approximation | capillary approximation | 3.77 |
| $E_B(V_n)$ | 0.30 | 0.67 | 1.29 | 2.02 | 2.07 |
| $E_B(C_n)$ | 0.09 | capillary | capillary | capillary | 0.41 |

MONTE-CARLO SIMULATIONS

For the simulations, an Event-based Kinetic Monte Carlo (EKMC) method is used, as implemented in JERK [2], [3], [4]. In this model, defects are considered as objects characterized by their space coordinates, nature (C_nV_m , C_nI_m , V_n and I_m in this work), shape (spherical here), mobility and dissociation rate. When mobile, these objects migrate and annihilate on their anti-defect (for I and V), or aggregate to form clusters. These diffusion processes are treated in a specific and efficient way: the details of the atomic transport are ignored and the jumps of the mobile species are bunched into trajectories complying with the laws of continuous diffusion. The probability that two defects meet can be extracted through a sampling of this probability distribution: the occurrence time (or delay) for a given event is thus determined by choosing random numbers. Only the events having a delay smaller than a prescribed time interval Δt are considered. The events are then processed in the order of increasing delays, and the list of events is continuously updated and reshuffled, by taking into account the defects which are created or which are annihilated. The time interval Δt which is a tuning

parameter of the model discussed elsewhere [4]; in our simulations, it is chosen in such a way that the fastest defect is able to travel over distances of the order of the simulation-cell size within Δt . It is thus a temperature dependent quantity.

Simulations were conducted on cubic cells, the edge of which is 200 a where 'a' stands for the lattice parameter. The Frenkel pairs I-V are introduced at random positions with a mutual distance equal to 4 a. Following the experimental set up, the isochronal annealings consist in raising the temperature by ΔT ($= 0.03$ T) and maintaining the sample at that temperature during 300 s [5].

To obtain resistivity plots from the defect population, we assume that resistivity is proportional to the remaining number of I and V, without discriminating between isolated defects and clustered ones. The resistivity difference between an isolated defect and the same defect embedded in a cluster is indeed expected to be significant only for large clusters. Moreover, experiments do not show any resistance change associated with the trapping of self-interstitials by carbon impurities. On the contrary, experimental evidences suggest that the resistivity of V-C complex is definitely lower than that of independent V and C defect. We therefore used the value reported in [5] i.e. $\rho_{V-C} = 0.78 \times 10^{-11}$ Ωm . Finally, since ab-initio calculations show that C atoms do not cluster as compact structures, we assume that no resistivity change results from the formation of carbon clusters. Our model will therefore not reproduce the "pure carbon" effect (clustering of C atoms) evidenced by *Takaki et al.* [5].

RESULTS AND DISCUSSION

Low temperature range ($T < 250K$)

We will first focus on the low temperature range (before stage III), where we expect to see mainly the influence of interactions between carbon and interstitials, since the related activation energies are weaker than the migration energy of vacancies, driving stage III.

We present our results together with the experimental observations:

- Stage I_{D2} is not affected by carbon doping: confirmed by the simulations;
- The recovery related to stage I_E is reduced, and a nearly complete suppression for the highest carbon content is observed. This effect was interpreted in [5] by the trapping of self-interstitial on carbon atoms, which prevents their recombination with immobile vacancies; this assumption is substantiated by the results of the simulations where the drop of the 'I' population around 130K is indeed accompanied by an increase of I-C and $I_2-C + I_3-C$ populations.
- A new peak is detected around 160K, the position of which depends neither on the irradiation dose nor on the carbon content: it was interpreted as the emission of self-interstitials from I-C complexes [5]. The effective activation energy is found equal to 0.43 eV. In the simulations, the I-C population starts to decrease around

150K giving rise to a new peak with an activation energy calculated ab-initio and equal to

$$E_M^I + E_b^{I-C} = 0.43 + 0.12 = 0.45 \text{ eV}$$

in good agreement with the experimental value of 0.43 eV.

- Stage II observed around 165K in pure iron and interpreted as the elimination of mobile interstitial clusters (I_2 , I_3) is no longer detected [5]. In the simulations, the disappearance of stage II is explained by the trapping of I_2 and I_3 on carbon atoms through the formation of I_2-C and I_3-C ;
- At higher carbon content and irradiation doses, a new small stage is detected around 185K, interpreted as the break of small (multiple) carbon-interstitial complexes IC_n ; in the simulations the I_2-C and I_3-C populations decrease above 185K by detrapping of I_2 and I_3 from these complexes, thus giving rise to a newly observed peak. Here, JERK's interpretation is slightly different from that invoked by Takaki [5]: the new peak is not due to the emission of I from complexes IC_n , but rather to the emission of I_2 and I_3 from complexes I_nC followed by their elimination.

We note that all the qualitative features observed in experiments are successfully reproduced. The positions of the peaks are in reasonable quantitative agreement with the experimental stages (black arrows for pure iron; red-dotted arrows for C-doped iron) as depicted in figure 1.

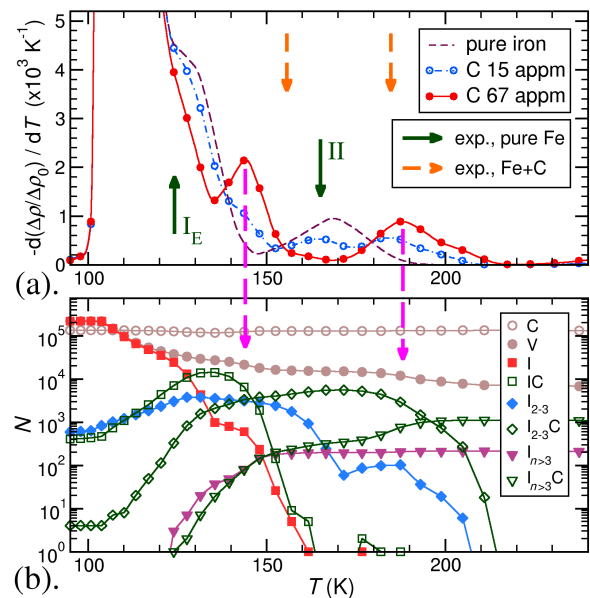


Figure 1: Resistivity recovery and defect population evolution during isochronal annealings (range of lower temperatures).

a)* dashed curve: Simulation for pure iron
* continuous curve with dots: simulation for carbon doped iron

Downwards unlabelled arrows indicate the experimental positions of peaks in carbon doped sample.

Downward dashed arrows from a) to b) indicate that the peak position is independent of carbon content.

b) Associated population evolution for 67 ppm C

High temperature range ($T > 250\text{K}$)

In the high temperature range, we expect to observe the influence of vacancy-carbon interactions and carbon migration.

- Carbon doping influences the stage III recovery process: at a given irradiation dose, the peak position is shifted toward lower temperatures, and the measured reaction order is lowered from ~ 2 to ~ 1 . The shift in temperature decreases with increasing dose, and becomes very small ($\Delta T \sim 5\text{K}$) at the highest one (200×10^{-6} dpa). This effect was attributed to the trapping of mobile vacancies by immobile carbon atoms and to the formation of V-C complexes. In this case, the drop in resistivity is not associated with a defect annihilation: it implies that the specific resistivity of the V-C complex formed during this stage is necessarily lower than the sum of the resistivities of the isolated defects. A value of $\rho_{VC} = 0.78 \times 10^{-11} \Omega\text{m}$ is reported and is used in our simulations.

This interpretation is verified by the simulations and explains both the shift in temperature of the peak and the change in the order of reaction, since for all configurations to be considered, carbon atoms are in large excess compared to the remaining self-defects at these stages of the annealing.

- An additional characteristic recovery stage appears at 340 K for Fe+C 67 appm and at 360 K for Fe+C 15 appm. The position of this stage depends only on carbon concentration, and not on the irradiation-induced defect concentration. In simulations the new stage near 350 K is then clearly related to carbon migration, leading to the formation of V-C₂ complexes through the trapping of mobile carbon atoms by immobile V-C complexes. Here again it is necessary to assume a specific resistivity for VC₂ complexes, in order to reveal the peak related to C migration. Moreover, we note that V-C complexes are turned into VC₂ *before* they can dissociate: this seems to indicate that such experiments will never give access to the V-C binding energy.

- Above 400 K, carbon doping introduces a more pronounced stage near 560 K, attributed to the decomposition of VC_m complexes formed as a result of carbon migration; the measured activation energy is $Q = 1.65 \text{ eV}$. In the simulations, the stage after 400 K appears to be related to the dissociation of VC₂ complexes, and the consequent elimination of the emitted vacancies on available sinks (the large interstitial clusters in our simulations). The significant difference between numerical and experimental peak positions seems to point toward an under-estimation of the VC-C binding energy by the ab-initio calculations.

CONCLUSIONS

The association of ab-initio calculations and EKMC simulation technique appears very promising: ab-initio yields the microscopic parameters for characteristic energies (formation, binding, migration) of defect and defect clusters and the EKMC technique is able to

incorporate all these results into an efficient package in order to propose a consistent scenario of defect elimination at macroscopic scale. As a consequence many old experimental results which have remained unexplained or insufficiently explained during the last decades can today be numerically simulated to check the robustness of the atomistic mechanisms at work.

Many of the explanations proposed previously by experimentalists are confirmed, namely the qualitative effect of carbon impurity on the trapping of self-defects (vacancy or interstitial types); if the lower temperatures annealing stages are correctly reproduced (at the expense of some minor changes: for instance, role of I_nC clusters instead of IC_n for stages below stage II), some discrepancies still remain at the higher temperatures where the vacancy defect becomes mobile. These discrepancies point toward an intrinsic difficulty of ab-initio techniques for predicting the properties of defects of vacancy type.

REFERENCES

- [1] C. C. Fu, J. Dalla Torre, F. Willaime, J. L. Bocquet, and A. Barbu, Nature Mat. 4, 68 (2005)
- [2] J. M. Lanore, Rad. Effects 22, 153 (1974)
- [3] F. Maurice and N. V. Doan, Simulation de l'évolution de populations de défauts dans un cristal par la methode de Monte Carlo (Technical Report CEA-R-5101, 1981)
- [4] J. Dalla Torre, J.L. Bocquet, N. V. Doan, E. Adam, and A. Barbu, Phil. Mag. 85, 549 (2005)
- [5] S. Takaki, J. Fuss, H. Kugler, U. Dedek, and H. Schultz, Rad. Effects 79, 87 (1983)

TASK LEADER

Jean-Louis BOCQUET

DEN/DMN/SRMP
CEA-Saclay
F-91191 Gif-sur-Yvette Cedex

Tel. : 33 1 69 08 54 62
Fax : 33 1 69 08 68 67

e-mail : jean-louis.bocquet@cea.fr

Task Title: RULES FOR DESIGN, FABRICATION, INSPECTION UPDATE DATA BASE AND APPENDIX A OF DEMO-SDC

INTRODUCTION

Eurofer is a reduced activation ferritic / martensitic steel that has been selected as the European reference structural material for ITER Test Blanket Modules and DEMO reactor. Several industrial heats of this steel have been produced and tested under EFDA's Tritium breeding and materials field / materials development tasks. The ultimate goal of these tasks is to propose materials properties allowable for design and licensing of components fabricated with the Eurofer steel.

This report presents a summary of the work done during the year 2006 at our Association on this task. The work done is also part of an international collaboration, coordinated under the fusion materials implementing agreement of the International Energy Agency (IEA). The main objective of the task is to collect, validate and harmonize the results of Eurofer steel, in continuation of the earlier work done on the conventional 9Cr-1Mo steel and the RAFM steel grade produced in Japan (F82H), and propose materials properties allowable through an Eurofer steel dedicated Appendix A.

2006 ACTIVITIES

All actions and deliverables foreseen under the terms of the task have been fulfilled. The database of Eurofer steel has been updated, particularly with higher dose irradiation results and results obtained from tests on bar products of Eurofer97-2.

With the addition of the new Eurofer steel data in 2006, the collection of relational databases for RAFM steels contains:

- Products database: 579 records
- Compositions database: 478 records
- Tensile database: 1257 records
- Impact database: 1787 records
- Impact plots: 161 records
- Creep database: 233 records
- Fatigue database: 262 records
- Fracture toughness database: 352 records, mostly for Eurofer steel, including 8 Master Curves.
- A few fatigue crack propagation test results
- Summary records for all databases

A CD-Rom containing the Runtime solution version 5, linking all above databases, as well as, the updated Appendix A reports has been issued.

The content of the Appendix A report is now well enriched with data on EB, TIG and diffusion bonded joints allowing a comprehensive evaluation of these joints along with the base metal. Also with the availability of high dose irradiation results, precision of extrapolation of mechanical

properties to higher doses is increased. Further improvements in the high neutron irradiation dose effects are expected when the results from second set of specimens irradiated in Bor 60 become available (70 dpa).

However, there are two areas of concern. One is the surprising weakness of Eurofer97-2 bar products. As shown in figures 1 and 2, tensile test results of Eurofer97-2 heats are situated below the average curve of the Eurofer 97 heats, with yield stress values even below the minimum curve.

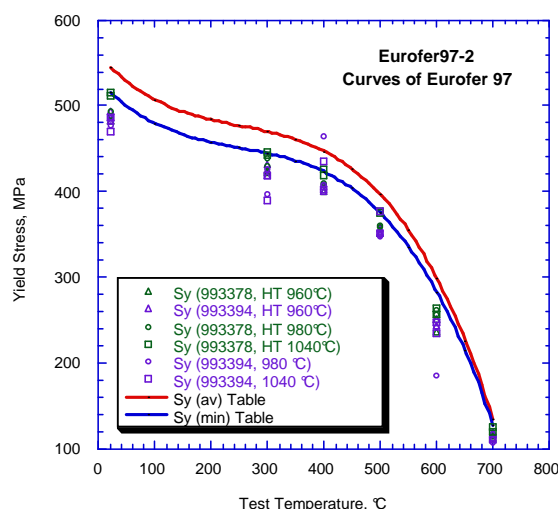


Figure 1: Yield stress of Eurofer97-2 (bar, L) in the as received state (960°C/90 min + 750°C/240 min), in 2 additional solution heat treatments (980 and 1040 °C) (FZK data), compared with the average and minimum curves established for Eurofer 97

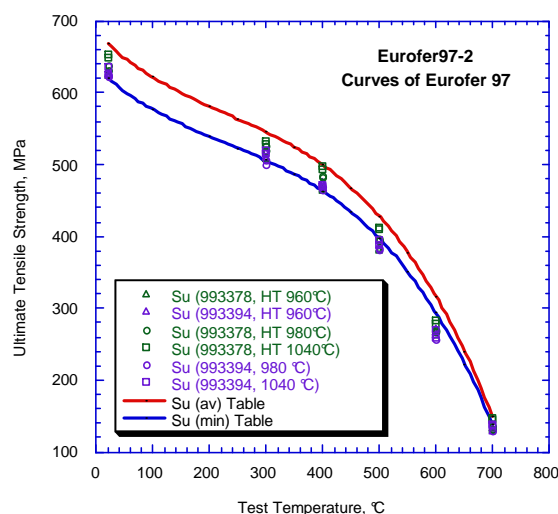


Figure 2: Ultimate tensile strength of Eurofer97-2 (bar, L) in the as received state (960°C/90 min + 750°C/240 min) and in 2 additional solution heat treatments (980 and 1040 °C) (FZK data), compared with the average and minimum curves established for Eurofer 97

Table 1 shows small deviations from the specified chemical composition ranges for 2 or 3 elements, but this is unlikely to have such an important effect. Besides, early results from the plate products of Eurofer97-2 show higher strengths.

Table 1: Specified compositions for F82H and Eurofer 97 steels and measured compositions for 2 heats of Eurofer97-2 (IMF/FZK). All compositions are in wt.%, unless otherwise stated. Target values in []

| Elements | F82H Steel | Eurofer 97 Steel | Eurofer97-2 (IMF/FZK) Heat 993378 – Heat 993394 | |
|----------|------------|-----------------------|--|------------|
| | | | | |
| Cr | 7.7 | 8.5 – 9.5 [9.0] | 9.01 | 8.95 |
| C | 0.09 | 0.09 – 0.12 [0.11] | 0.106 | 0.106 |
| Mn | 0.16 | 0.20 – 0.60 [0.40] | 0.512 | 0.544 |
| P | 0.002 | < 0.005 | < 0.00015 | < 0.00015 |
| S | 0.002 | < 0.005 | < 0.001 | < 0.001 |
| V | 0.16 | 0.15 – 0.25 | 0.247 | 0.350 |
| B | 0.0002 | < 0,001 | 0.0007 | 0.00024 |
| N2 | 0.006 | 0.015 – 0.045 [0.030] | 0.011 | 0.036 |
| O2 | (0.01) | < 0,01 | 0.0009 | 0.0012 |
| W | 1.94 | 1.0 - 1.2 [1.1] | 1.125 | 1.109 |
| Ta | 0.02 | 0.06 - 0.09 | 0.134 | 0.197 |
| Ti | 100 ppm | < 0.01 (100 ppm) | | |
| Nb | 1 ppm | [<10 ppm] | < 0.000049 | < 0.000042 |
| Mo | 30 ppm | [< 50 ppm] | < 0.001 | < 0.00017 |
| Ni | 200 ppm | [< 50 ppm] | 0.0113 | 0.0157 |
| Cu | 100 ppm | [< 50 ppm] | 0.0021 | 0.0030 |
| Al | 30 ppm | [<100 ppm] | 0.0194 | 0.0285 |
| Si | 1100 ppm | < 500 ppm | | |
| Co | 50 ppm | [< 50 ppm] | 0.0054 | 0.0075 |
| Sn | (< 20 ppm) | As+Sn+Sb+Zr < 100 ppm | 0.00033 | < 0.00028 |
| As | (< 50 ppm) | As+Sn+Sb+Zr < 100 ppm | <0.001 | <0.001 |

A full assessment of the Eurofer97-2 products will be carried out when more results become available. In case the cause of dispersion is heat-to-heat variation or differences in thermo-mechanical treatments, then recommended stress intensity allowable would be revised to cover such variations.

The second area of concern is the ODS steels. The results from tests performed on ODS steel products are still inadequate for Appendix A type analysis.

Those few results available have many variables (different products, different compositions, different thermo-mechanical treatments, different testing procedures ...) to allow a minimum reliable analysis. Definition of one or two agreed referenced products and subsequent characterization without additional modification in each laboratory is needed.

CONCLUSIONS

Interim Structural Design Criteria / Appendix A for Eurofer steel and its related databases have been updated. The results from tension tests performed on new Eurofer heat (Eurofer97-2) bar products are situated well below the Eurofer 97 heats. Evaluation of other Eurofer97-2 products is recommended before a definitive conclusion is drawn.

REPORTS AND PUBLICATIONS

F. Tavassoli, "Interim Structural Design Criteria (ISDC), Appendix A Material Design Limit Data: A3.S18E Eurofer Steel", CEA/DMN/Dir/2006-05/A, Dec. 2006

TASK LEADER

Farhad TAVASSOLI

DEN/DMN/Dir
CEA-Saclay
F-91191 Gif-sur-Yvette Cedex

Tel. : 33 1 69 08 60 21
Fax : 33 1 69 08 80 70

e-mail : tavassoli@cea.fr

Task Title: MODELLING OF IRRADIATION EFFECTS AB-INITIO STUDY OF He IN GRAIN BOUNDARIES IN α -IRON

INTRODUCTION

Ferritic steels play a central technological role as structural materials for future fusion nuclear reactors. One of the principal sources of their mechanical property degradation is the intergranular embrittlement, which can be caused by segregation of solutes at grain boundaries (GBs). In particular, fusion reactors produce high energy neutrons (~ 14 MeV) that interact with the structural material, which cause nuclear transmutations and create significant amount of helium. The formation of helium bubbles at GBs is known to lead to high temperature embrittlement. A quantitative description of the interaction of He atoms with grain boundaries is therefore essential. First principles calculations provide such information at atomic scale [1], [2], which is not directly accessible through experiments. The present calculations are based on the DFT-SIESTA code, (Spanish Initiative for Electronic Simulations with Thousands of Atoms: <http://www.uam.es/siesta>) [3], [4]. This methodology has been applied in 2004 to predict the migration of interstitial and substitutional He atoms in pure α -Fe, and their interaction with other He atoms and with vacancies [5]. In 2005, the same approach has been extended to the interaction between self-interstitials and He, and to the effect of carbon on the energetic of helium-vacancy clusters.

In 2006, ab-initio and empirical potential (E.P.) simulations have been performed to study the properties of representative symmetric tilt grain boundaries in α -iron. DFT-SIESTA code within the Generalised Gradient Approximation (GGA) is used to study the structural, energetic and magnetic properties of certain GBs in bicrystals which contain a few hundred atoms. The lowest energy binding sites for He at these GBs are also investigated. These ab-initio data are compared to MD results using similar and much larger systems. Such a comparison is required for the validation of the existing empirical potential and to fit new, improved ones. The necessity of MD simulations lay in their ability to study the finite temperature effects on these properties as well as providing an understanding of the size effects of simulation cells. The present study is the first step towards a predictive description of the segregation of He at GBs and their embrittling effects in the steels.

2006 ACTIVITIES

Method of calculation

In the present study we have considered two symmetric tilt grain boundaries with tilt axis (110): $\Sigma 3$ {112} and $\Sigma 3$ {111}. Supercells containing two identical GBs are used, and periodic boundary conditions are applied in all the

three directions, either parallel or perpendicular to the GB plane. Various simulation cell sizes have been tested in order to achieve a compromise between the convergence of relevant properties and the required computational time. All the following ab-initio results correspond to 192 atom cell simulations with 24 atomic layers parallel to the GB plane and 8 atoms per layer.

Properties of symmetric tilt grain boundaries

$\Sigma 3$ {112} is a coherent twin boundary in α -iron with low formation energy, whereas $\Sigma 3$ {111} has a higher formation energy and a larger volume expansion normal to the GB plane after full relaxation, which implies a larger excess volume according to Kurtz et al. [6]. A schematic representation of these GBs is shown in figure. 1 where spheres of different colors indicate atoms in alternating planes perpendicular to the tilt axis.

Formation energies of both $\Sigma 3$ GBs and of the corresponding free surface, as well as the cohesive energies of these GBs are shown in table 1. Results from various

ab-initio calculation conditions are shown: (1) the atoms are in their original positions (unrelaxed), (2) the forces of all the atoms are minimized keeping the original cell volume unchanged ($V=cte.$), and (3) the atomic positions and the shape and the volume of the supercell are optimized ($P=cte.$). Please note that in the case (3) the only relevant variation of the cell volume consists in a volume expansion perpendicular to the GB plane.

The unrelaxed interatomic distances at these GBs are the same as in the bulk, but the deviation of bond angles at the interface from the bulk values is larger in $\Sigma 3$ {111} than in $\Sigma 3$ {112}, which is coherent with the result that $\Sigma 3$ {112} has a smaller formation energy, and the difference between its unrelaxed and relaxed ($V=cte$) energies are much smaller than that of $\Sigma 3$ {111}. The stress relaxation perpendicular to the GB plane ($P=cte$) is relevant for ab-initio calculations, when the cell size is relatively small. The differences of GB formation energies between $V=cte$ and $P=cte$ calculations are about 8% for both $\Sigma 3$ {112} and $\Sigma 3$ {111} GBs.

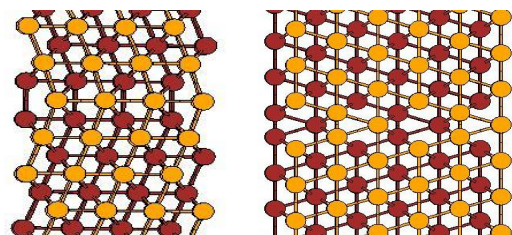


Figure 1: Schematic representations of the atomic structures of $\Sigma 3$ {112} (110) (left), and $\Sigma 3$ {111} (110) (right) symmetric tilt grain boundaries in α -iron. Spheres of different colors represent atoms in alternating planes perpendicular to the (110) tilt axis

The present ab-initio results are compared with those using empirical potentials. We have chosen two widely used interatomic potentials: the Finis Sinclair (FS) from Ackland et al. [7], and the EAM type from Mendeleev et al. [8]. Supercells containing 24 atomic layers and either 12 or 16 atoms per layer are used to simulate respectively $\Sigma 3$ {112} and $\Sigma 3$ {111} GBs. 3-dimensional periodic boundary conditions are applied, and only atomic positions are allowed for relaxation ($V=cte$). The agreement in GB reasonably good, the discrepancies in all cases are smaller than 20%.

This almost quantitative agreement is surprising since neither FS nor EAM potentials are central force potentials, and do not explicitly include angular terms. These potentials, however, significantly underestimate the formation energies of the free surfaces. As a consequence of this underestimation, the energetical stabilities of these GBs against brittle fracture determined by the GB cohesive energy are also underestimated as shown in table 1.

Figure 2 shows the deviations of interlayer distances after full relaxation ($P=cte$) from the unrelaxed ones ($\Delta d_{ij} = d_{ij} - d_0$). These deviations give indications about the range of the stress field around the GBs, and the minimum cell size required for the simulation. They are rather small in magnitude near a $\Sigma 3$ {112} GB, and have non negligible values in only 3 layers from the GB planes, which indicates that the present simulation cell is large enough to keep the two identical GBs in the same cell well separated. On the other side, the stress field is more long-ranged around $\Sigma 3$ {111}, and the deviations (Δd_{ij}) oscillate between positive and negative values. Although they are only 3% of the original value (d_0) for the middle layers between the two identical GBs in the same cell, it may be important to check the convergence of relevant GB properties using a larger simulation size. We want to point out that similar interlayer distance deviations are found using both the FS and EAM potentials. In addition, the present results are consistent with the estimation of Kurtz et al. [6] showing that the excess volumes vanish starting at 3rd and 8th layers from the $\Sigma 3$ {112} and the $\Sigma 3$ {111} GBs respectively.

We have also examined the local magnetic moments of atoms at different layers parallel to the GBs according to the Mulliken population analysis. Changes of local magnetic moments ($\Delta \mu_i$) with respect to the bulk value ($2.31 \mu_B$) near the free (112) surface and the $\Sigma 3$ {112} and $\Sigma 3$ {111} GBs are shown in figure 3.

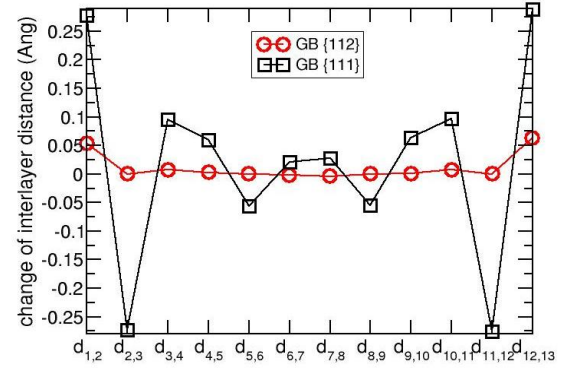


Figure 2: Changes of interlayer distances ($\Delta d_{ij} = d_{ij} - d_0$) after full relaxation ($P=cte$) with respect to the respective original unrelaxed distances for $\Sigma 3$ {112} and $\Sigma 3$ {111} GBs. The atomic layers 1 and 13 are the closest layers to the GBs

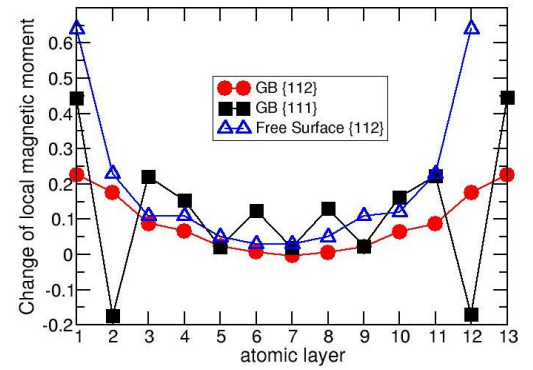


Figure 3: Change of local magnetic moment ($\Delta \mu_i$ in μ_B) with respect to that of a Fe atom in the bulk. Positive values indicate increase of magnetic moments

We note that the magnetic moments of atoms located at either a surface or an interface layer are increased due to the decrease of coordination [2], and in general, the values of $\Delta \mu_i$ closely follow the variation of interlayer distances in all cases (figure 2), i.e. an increase of the interatomic distance induces an enhancement of magnetic moment and vice versa. The modification of local magnetic properties near surfaces and interfaces may also contribute to induce changes of energetic and kinetic properties of point defects (e.g. vacancies and self-interstitial atoms) near these extended defects.

Table 1: Calculated formation energies of two symmetric tilt GBs (E_{GB}^f), formation energies of the corresponding free surfaces (E_{surf}^f), and the cohesive energies of the GBs (E_{GB}^{coh}), where $E_{GB}^{coh} = 2E_{surf}^f - E_{GB}^f$. The DFT-SIESTA values are compared with those resulting from a Finis Sinclair (F.S.) and Embedded Atom Model (EAM) potentials

| (j/m ²) | $\Sigma 3$ {112} | | | $\Sigma 3$ {111} | | |
|------------------------------|------------------|--------|---------|------------------|--------|---------|
| | SIESTA | FS [7] | EAM [8] | SIESTA | FS [7] | EAM [8] |
| $E_{GB}^f(\text{unrelaxed})$ | 0.49 | 0.48 | 0.38 | 4.15 | 6.86 | 5.81 |
| $E_{GB}^f(V = cte.)$ | 0.37 | 0.33 | 0.33 | 1.66 | 1.54 | 1.39 |
| $E_{GB}^f(P = cte.)$ | 0.34 | - | - | 1.52 | - | - |
| E_{surf}^f | 2.99 | 1.82 | 1.88 | 3.07 | 2.02 | 2.02 |
| E_{GB}^{coh} | 5.64 | 3.31 | 3.43 | 4.62 | 2.50 | 2.65 |

He in grain boundaries

In order to understand the behavior of He near the GBs, we have started investigating the energetic interaction between one atom of He and the $\Sigma 3$ ground boundaries.

The binding energies of a substitutional He at the interfacial and the 2nd layers, as well as the most favorable interstitial site found near the GBs are listed in table 2. The binding energy is defined as the energy difference between the situation when the He atom is substitutional in the bulk and far from a GB and when it is near the GB plane. Several features are interesting to point out:

- All the interactions are attractive according to the present ab-initio results, whereas interstitial sites are not energetically favorable near a $\Sigma 3$ {112} GB according to existing EP calculations [6].
- Both SIESTA and E.P. studies predict that He prefers to be close to the $\Sigma 3$ {111} GB with higher formation energy and larger excess volume than close to the $\Sigma 3$ {112} GB. Therefore, the relative stabilities of GBs may change in presence of He.
- Substitutional sites at the second layer are more favorable than those at the interfacial layer according to both ab-initio and E.P. calculations. This relative stability seems therefore too uncorrelated of the local magnetic environment.
- Interstitial sites are more favorable than substitutional ones at the GB plane, which suggest that He atoms may migrate easily via interstitial mechanisms parallel to the interface.

In order to understand the effect of He on the GB cohesion, we compared the binding energy of He with a given GB and that of He with the corresponding free surface following the thermodynamic theory of embrittlement by Rice and Wang [9]. According to this theory the potency of an impurity to increase (decrease) intergranular cohesion is a linear function of the difference in binding energies for that impurity at the GB and at the corresponding surface.

Since the He atoms tend to desorb from any free iron surface, and assuming that the binding energy between He and a free surface is the energy difference between the situation when He is substitutional in the bulk far from the surface and when it is at the surface, the resulting binding energy is about 4.22 eV i.e. the solution energy of He in bcc iron [5]. According to the values listed in table 2, this He-surface binding energy is much larger than any He-GB binding energy. He is therefore expected to decrease the GB cohesion in all cases.

Table 2: Fully relaxed (P=cte) binding energies between a helium atom and $\Sigma 3$ {112} or $\Sigma 3$ {111} GB. Values from the present SIESTA calculations are compared with those from E.P. simulations reported in [6]. Positive values indicate attractive interactions

| E ^b (eV/He) | He _{subs} 1 st layer | He _{subs} 2 nd layer | He _{int} |
|--------------------------|--|--|-------------------|
| SIESTA | | | |
| $\Sigma 3$ {112} | 0.02 | 0.44 | 0.13 |
| $\Sigma 3$ {111} | 0.33 | 1.35 | 1.24 |
| E. P. (Kurtz et al. [6]) | | | |
| $\Sigma 3$ {112} | - | 0.2 | -1.45 |
| $\Sigma 3$ {111} | 0.3 | 0.8 | 0.66 |

CONCLUSIONS

The following conclusions can be drawn from the present ab-initio calculations on the energetic, structural and magnetic properties of symmetric tilt grain boundaries in α -Fe and on the effect of He on these GBs:

- Good agreements are found between ab-initio and two existing E.P. results on the formation energies of $\Sigma 3$ GBs, but the both empirical potentials underestimate the free surface energies and consequently the GB cohesive energies.
- An enhancement of local magnetic moments in Fe atoms at the interfaces is noted consistent with the increase of their interatomic distances.
- The interactions between He and these symmetric tilt GBs are attractive. Qualitative and quantitative discrepancies are found between ab-initio and empirical potential results on He-GB binding energies.
- He atoms prefer to be in GBs with large excess volume in agreement with existing E.P. studies.
- He atoms tend to occupy interstitial rather than substitutional sites close to the GB planes, which suggest that He may migrate easily via interstitial mechanisms along the interfaces.

REFERENCES

- [1] R. Janisch and C. Elsässer, Phys.Rev. B, 67, 224101, (2003)
- [2] R. Wu, A.J. Freeman and G.B. Olson, Phys.Rev. B, 53, 7504, (1996)
- [3] J.M. Soler, E. Artacho, J.D. Gale, A. Garcia, J. Junquera, P.Ordejon and D. Sanchez- Portal, J. Phys. Cond. Matter 14, 2745 (2002)
- [4] C.C. Fu, F. Willaime and P. Ordejon, Phy. Rev. Lett. 92, 195503 (2004)
- [5] C.C. Fu and F. Willaime, Phys. Rev. B, 72, 064117, (2005)
- [6] R.J. Kurtz and H.L. Heinisch, J. Nucl. Mater, 329-333, 1199, (2004)
- [7] G. J. Ackland, D. J. Bacon, A. F: Calder, and T. Harry, Phil. Mag A 75, 713 (1997)
- [8] M. I. Mendeleev, S. Han, D.J. Srolovitz, G.J. Ackland, and D.Y. Sun, M. Asta, Phil. Mag. 83, 3977-3994 (2003)
- [9] R. J. Rice, and J.-S. Wang, Mater. Sci, Eng. A, 107, 23 (1989)

TASK LEADER

Chu Chun FU

DEN/DMN/SRMP
CEA-Saclay
F-91191 Gif-sur-Yvette Cedex

Tel. : 33 1 69 08 29 32
Fax : 33 1 69 08 68 67

e-mail : chuchun.fu@cea.fr

Task Title: MODELLING OF IRRADIATION EFFECTS AB-INITIO INVESTIGATION OF SCREW DISLOCATIONS IN IRON

INTRODUCTION

Ferritic steels are proposed as structural material in fusion reactors. The specificity of the plastic behavior of body-centered cubic (bcc) metals at low temperature is attributed to the non-planar core structure of $\frac{1}{2} \langle 111 \rangle$ screw dislocations which induce a high lattice-friction Peierls stress. The goal of this subtask is to obtain a quantitative description of the structure and properties of these dislocation cores in bcc iron by performing first principles electronic structure calculations. These calculations are carried out within the DFT framework using localized basis functions as implemented in the SIESTA code. This methodology was set up and validated in 2003-2005 for the study of point defect, defect clusters, and defect complexes, such as helium-vacancy clusters. In 2006, this approach has been extended to the study of dislocations.

2006 ACTIVITIES

METHODOLOGY

This work is based mainly on first principles DFT-GGA electronic structure calculations performed with the SIESTA code [1]. In the first part, the generalized stacking faults are studied, their properties being closely related to that of the dislocation cores. We have investigated the effect of basis set and exchange-correlation functional. The properties of dislocation cores are then investigated using two geometries: (i) the cluster approach with a single dislocation in a cylinder with fixed atoms at the free surfaces; and (ii) a periodic array of dislocation dipoles. For the latter the cell geometry has been optimized for two dipole arrangements. Some insight into the mobility of the dislocation is gained by calculating the Peierls barrier, i.e. the energy barrier between two consecutive local minima of the energy landscape seen by a straight dislocation. The performances of empirical potentials for iron, recently proposed by Mendeleev et al. and by Dudarev et al., are investigated against the present results.

GENERALIZED STACKING FAULT ENERGIES IN IRON

The gamma surfaces are obtained by cutting a perfect crystal and displacing the two parts relative to each other in a direction parallel to the cut plane (figure 1(a)). For each displacement vector the atomic positions are relaxed only in the direction perpendicular to the cut plane. As we vary the fault vector, the excess energy generates a surface, which represents the energies of "generalized" stacking faults. We have performed a comparison between LDA and GGA functionals and the validation of SIESTA with a plane wave code (PWSCF). The $\{110\}$ γ -lines obtained

within DFT and with the Mendeleev potential [2] suggest a non-degenerate core structure according to the Duesbery-Vitek criterion [3] while a degenerate core structure is expected for the Dudarev potential [4] (see figure 1(b)).

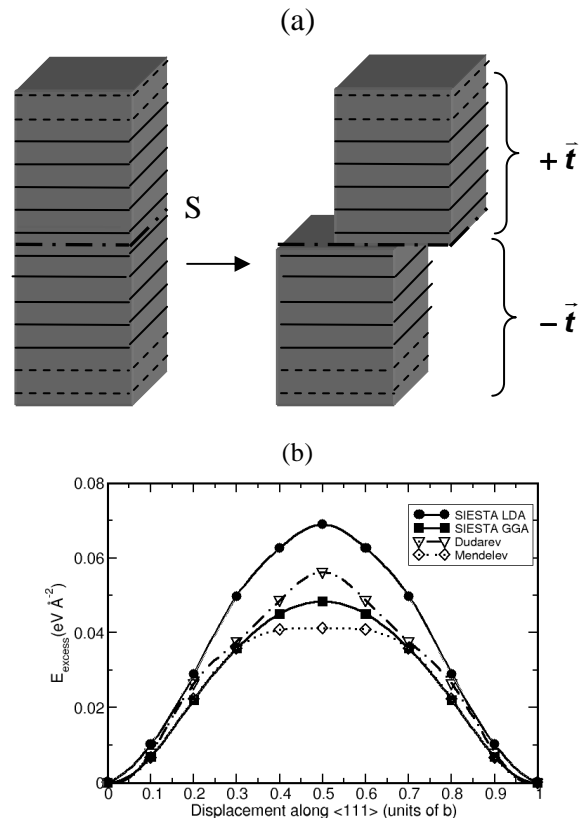


Figure 1: (a): Schematic representation of the procedure for the calculation of generalized stacking fault energy.

(b): $\langle 111 \rangle \{110\}$ gamma lines in iron; comparison between the SIESTA results obtained using either LDA or GGA for the exchange correlation energy, and two empirical potentials proposed respectively by Mendeleev et al. and by Dudarev and Derlet

CELL ARRANGEMENTS AND BOUNDARY CONDITIONS FOR DISLOCATION CORE CALCULATIONS

For the calculations on dislocation cores, we compared the two cell geometries proposed in the literature: the cluster approach [5] and the periodic array of dislocation dipoles [6]. Within the cluster model, a single dislocation is placed at the centre of a "cylinder"; the surface atoms are fixed to the positions predicted by the elasticity theory, while the inner ones are relaxed. In the dipole approach, we compared two arrangements: a triangular and a square periodic array of dislocations (figure 2). In the triangular geometry, the dislocations are positioned on a honeycomb lattice, that preserves the three-fold symmetry of the bcc lattice in the $\langle 111 \rangle$ direction. The square lattice corresponds to a quadrupolar distribution. We have

optimized the cell geometry by adding tilt components to the cell vectors in order to accommodate the plastic strain introduced by the dislocation dipole. These tilt components are deduced from elasticity calculations; the atomistic calculations confirm that they indeed yield vanishing shear stress component.

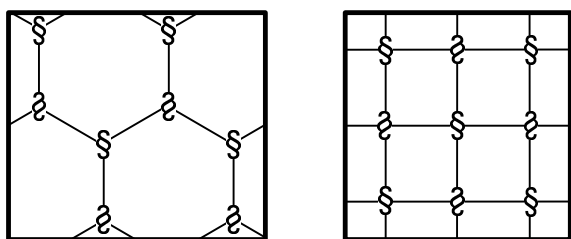


Figure 2: Schematic representation of the two types of periodic arrays of screw dislocation dipoles investigated in the present study: (a) the triangular and (b) the quadrupolar arrangements

CORE STRUCTURE OF $\langle 111 \rangle$ SCREW DISLOCATION

DFT results show that the relaxed structure of the easy configuration of $\langle 111 \rangle$ screw dislocation does not lead to any broken symmetry about the $\langle 110 \rangle$ axes or any spreading along the $\langle 211 \rangle$ directions, so that the easy core structure exhibits a non-degenerate core configuration in agreement with previous calculations [7] and as expected from the γ -line calculations. The degenerate easy core structure is found to be unstable, while the hard core is found to be metastable with an energy increase with respect to the easy configuration of about 50 meV/b. These relaxed core structures are found to be close to the elasticity theory, the small deviation from the prediction of elasticity can be illustrated by subtracting the elastic displacement field (see figure 3). This deviation can also be seen on the edge component maps, i.e., the displacement field in the $\{111\}$ plane. The magnetic moment of the three core atoms is reduced by $0.2 \mu_B$ from its bulk value ($2.3 \mu_B$) for both the easy and hard cores. The cluster and dipole approaches are in very good quantitative agreement with each other.

The Mendelev potential exhibits a non-degenerate core structure - as expected from the Duesbery-Vitek criterion - in relatively good qualitative agreement with DFT results with somewhat significantly smaller edge components. As expected from the γ -line calculations, the Dudarev-Derlet potential reveals a degenerate core structure at variance with DFT results.

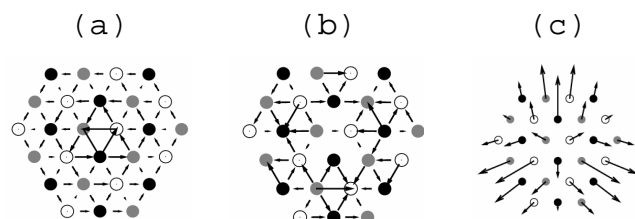


Figure 3: Core structure of $\langle 111 \rangle$ screw dislocation in iron obtained with DFT after relaxation. (a): differential displacement map ; (b): same as (a) after subtraction of the elastic field and magnification by a factor of 20 ; and (c): displacement in the (111) plane – or edge component – shown with a magnification factor of 50

CELL SIZE DEPENDENCE

The cell-size dependence within both the dipole and cluster approaches have been investigated. Within the dipole approach, the energy increase as the cell size increases is essentially given by the elastic energy, as obtained from a Madelung summation based solely on the values of the elastic constants. We analysed in detail the origin of the small deviation from the elasticity behaviour. We showed that it can be attributed to long range core-core interactions due to the edge components. Within the cluster approach we showed using empirical potentials that an excellent agreement is obtained between a cell containing 161 atoms / b and an infinitely large cell for the energy increase at the halfway position for the Peierls barrier calculation.

PEIERLS BARRIER

We successfully calculated the Peierls barrier using the drag method, both in the cluster and the dipole approaches. The dislocation is initially set on an easy core position and it is moved to the next easy core configuration along the $\langle 211 \rangle$ direction. DFT results yield a single hump barrier, with a height of ~ 30 meV/b. The barrier displayed by the Mendelev potential is quite different, with a camel hump shape; at the halfway position, the core spreads between two easy core positions while within DFT it exhibits a nearly hard core structure. These results suggest that the Mendelev potential may not be very appropriate for quantitative studies on the dislocation mobility in iron. We performed the same calculations within the dipole approach using Mendelev potential. The results obtained using the square-arrangement are in excellent agreement with the cluster-approach results.

CONCLUSIONS

The following conclusions can be drawn from the present DFT-GGA calculations performed on generalized stacking faults and dislocation cores in iron:

- We successfully set up two procedures for the study of dislocation properties, within the cluster and the dipole approaches. An excellent agreement is obtained between these two methods, both for the core structure and the Peierls barrier.
- The core structure, within DFT calculations, is found to be non degenerate, as expected from the shape of the generalized stacking fault energy surface, and at variance with predictions from most empirical potentials (except the Mendelev potential).
- The cell-size dependence of the excess energy in dipole calculations is dominated by elastic effect, but significant long range, anisotropic core-core interactions have been evidenced.
- The Peierls barrier has been calculated. It has a single hump, 30 meV high.
- The best available potential for iron, the Mendelev potential, shows qualitative discrepancies with the DFT results as regard to the deviation from linear elasticity of the core structure and the shape of the Peierls barrier.

REFERENCES

- [1] J.M. Soler, E. Artacho, J.D. Gale, A. Garcia, J. Junquera, P.Ordejon and D. Sanchez- Portal, *J. Phys. Cond. Matter* 14, 2745 (2002)
- [2] M. I. Mendeleev, S. Han, D. J. Srolovitz, G. Ackland, D. Y. Sun and M. Asta, *Philos. Mag.* 83, 3977 (2003)
- [3] M. S. Duesbery and V. Vitek, *Acta. Mater.* 46, 1481 (1998)
- [4] S. L. Dudarev and P. M. Derlet, *J. Phys.: Condens. Matter* 17, 7097 (2005)
- [5] C. Woodward and S. I. Rao, *Phys. Rev. Lett.* 88, 216402 (2002)
- [6] W. Cai, V. V. Bulatov, J. Chang, J. Li and S. Yip, *Philos. Mag.* 83, 539 (2003)
- [7] S. L. Frederiksen and K. W. Jacobsen, *Philos. Mag.* 83, 365 (2003)

REPORTS AND PUBLICATIONS

- [8] L. Ventelon and F. Willaime, *Core Structure and Peierls Potential of Screw Dislocations in α -Fe from First Principles: Cluster versus Dipole Approaches*, submitted for publication

TASK LEADER

François WILLAIME

DEN/DMN/SRMP
CEA-Saclay
91191 Gif-sur-Yvette Cedex

Tel. : 33 1 69 08 28 10
Fax : 33 1 69 08 68 67

e-mail : francois.willaime@cea.fr

**Task Title: MODELLING OF IRRADIATION EFFECTS
RECOVERY FOLLOW-UP BY ELECTRICAL RESISTIVITY
OF VERY THIN SAMPLES IRRADIATED WITH THE JANNUS
MULTI-ION-BEAM FACILITY**

INTRODUCTION

The main objective of this task is to assess the feasibility of damage recovery follow-up by electrical resistivity on irradiated thin iron samples. Indeed, electrical resistivity measurement carried out on metallic samples during and after irradiation at low temperature is an efficient method to obtain information about the elementary defects induced by irradiation. In addition, it is very valuable to validate calculation performed at the atomic scale by ab-initio methods or by using empirical potentials. However, intensively used in the seventies in the case of irradiations with electrons that induce isolated Frenkel pairs (FP), this method is difficult to implement for heavy ion irradiations that, as neutron irradiations, result in the production of point defects in displacement cascades. This is due to their low penetration in iron and steels (only some microns). Consequently only very thin samples can be used. This induces two problems:

- Possible surface effects on resistivity measurement.
- Difficulty to prepare and handle such thin samples.

In spite of these difficulties, this type of experiment is very important to assess important issues as the mobility of small interstitial clusters created in the core of the displacement cascades. To carry out this task, we first performed a bibliographic study of damage production and damage recovery follow-up by electrical resistivity on irradiated thin iron samples. Then a bibliographic study of the effect of surfaces in the case of very thin sample has been carried out. Finally, this effect has been quantitatively evaluated in the experimental conditions that will prevail in the ion irradiation JANNUS facility that will be operative in Saclay by the end of 2007.

2006 ACTIVITIES

ELECTRICAL RESISTIVITY STUDY OF THE PRODUCTION AND PROPERTIES OF POINT DEFECTS

The electrical resistivity was used very early in the field of irradiation of metallic solids. A great amount of work was carried out using these techniques during the sixties and the seventies. Performed at low temperature, electrical resistivity gave a lot of information on the formation and properties of point defects at a time when numerical calculations were practically impossible. Nowadays, most of the experimental equipments unfortunately do not exist any more or are out of age. It is a pity if we consider that

the resistivity, thanks to its extreme sensitivity, is one of the very useful methods for validation of multi-scale numerical calculations at a very elementary level.

Electrical resistivity for assessing the formation of point defect under irradiation

In these studies, the resistivity measurement is carried out during continuous irradiation at low damage rate and very low temperature, not only to minimise the phonon contribution to resistivity, but also in order to prevent as far as possible the mobility of defects. The great majority of irradiations were carried out with 1 to 3 MeV electrons. The reason is that electrons produce a very simple damage as it is only made of isolated Frenkel pairs (no cascades) and that the penetration of electrons of these energies is high, allowing to use samples up to some hundreds thick with a relatively good homogeneity in term of damage rate.

From the electrical resistivity curve versus time, several important quantities can be obtained:

- The cross section of point defect creation if the resistivity per defect is known,
- The threshold energy for FP production,
- The FP recombination volume.

Electrical resistivity recovery after electron irradiation for assessing point defect mobility

Isochronal resistivity recovery allows studying reactions between defects and consequently their mobilities. Irradiations are usually carried out at liquid hydrogen or helium temperature in order to produce immobile FPs at concentrations within the range 1-100 ppm. Isochronal annealings of typically 10 minutes are carried out; the temperature is increased after each annealing period. The resistivity measurements are performed at 4K between each isochronal annealing.

Every rapid drop of the resistivity curve as a function of temperature corresponds to a reaction between defects due to the activation of the mobility of at least one defect. The derived curve is usually preferred for obvious reasons. Each peak corresponding to a rapid decrease in resistivity is usually called a stage.

The resistivity, being a global method, is unable to determine the physical phenomena associated to each peak. Based on other experimental methods or atomistic calculations and intuition, some reaction were attributed to a given peak. The properties of the peak, as the position change with the initial FP concentration, give precious insights on the involved reactions.

Thanks to the huge increase of the capability of computer, it is now possible to calculate the recovery from first principle in simple case. Such a multi-scale calculation was carried out recently for the first in the case of electron irradiated

ultra pure iron [2], [5]. It is based on ab-initio methods for the defect properties and on a Monte-Carlo method for the kinetic. The initial interpretation [4] is only partially confirmed. For instance, the so called stage II must not only be attributed to the di-interstitial mobility but also to cluster of three interstitials. Furthermore, the migration of interstitial cluster for $n>3$ is not required to reproduce the experiments.

IRRADIATION WITH PARTICLES INDUCING DISPLACEMENT CASCADES

Particles inducing cascades are neutrons or ions. The structure of the primary damage under cascade conditions is very different from the one obtained under electron irradiation. Homogeneous in space and time under electron irradiation, it is extremely heterogeneous under cascade conditions. In addition, in the latter case, not only isolated point defects are generated, but also small point defect clusters. Molecular dynamics simulations predict a very large mobility of these clusters. However, if such a large mobility is considered in kinetics modelling of the microstructure evolution under continuous irradiation at one third of the melting temperature, the simulated results are in total disagreement with experimental observations. The electrical recovery after irradiation at 4K is certainly a very good method to address this important issue.

The range of neutrons in materials being very large, there is no problem related to the effect of sample size on the resistivity. The major difficulties are to have access to an experimental device allowing carrying out irradiation at 4K in the core of a nuclear reactor. As far as we know there is no more such a device available. In addition, impurities produced in nuclear reactions can affect the behaviour.

Irradiations with ions that create also displacement cascades, as these that will be available in the JANNUS facility, are in principal considerably easier to perform. Unfortunately the ion ranges in material of interest are limited to some microns. Table 1 gives typical ranges in iron of ions that will be available in JANNUS.

Table 1: Typical characteristics of ion available in the JANNUS facilit.

| Ion | H | He | C | N | Fe | Au |
|--------------|----|----|-----|-----|-----|-----|
| Energy (MeV) | 3 | 6 | 12 | 15 | 25 | 48 |
| Range (μm) | 35 | 12 | 4.7 | 4.9 | 3.4 | 4.2 |

But for H ions (protons), particles creating mainly isolated Frenkel pairs as electrons or He ions that create very small cascades, the ranges of ions are of the order of 4 μm or smaller. It is interesting to notice that, but for iron ions in steel, ions are implanted and consequently must be seen as implanted impurities. This problem can be avoided if the thickness of the sample is significantly smaller than the range. At such a low thickness, the possible effect of the surfaces on the resistivity measurements is an important issue. Indeed, if the probability for a conduction electron to be scattered by the surfaces is of the same order of magnitude as the one to be scattered on a defect, the resistivity must be corrected.

SURFACE EFFECT CORRECTION OF THE ELECTRICAL RESISTIVITY MEASUREMENT IN IRRADIATED THIN METALLIC SAMPLES

The surface effect correction is based on the Fuchs-Sondheimer theory [3]. It is developed within the framework of the Boltzmann transport theory and the relaxation time approximation. For a thin foil, the electron distribution function is now dependant on the distance at the surfaces.

This theory shows that the ratio of the resistivity change of the thin foils per unit concentration of defects to the resistivity change of the thin bulk per unit concentration of defects is given by:

$$\frac{d\rho^f}{d\rho^b} = Q(x)$$

With: $Q(x) = \frac{d}{dx}\Phi(x)$, $x = \frac{a}{k}\rho^b$, a the sample thickness, $k = \rho^b\lambda$ and λ the mean free path.

The $\Phi(x)$ function is given by:

$$\frac{1}{\Phi(x)} = \frac{1}{x} - \frac{3}{2x^2} (1-p) \int_1^\infty \left(\frac{1}{u^3} - \frac{1}{u^5} \right) \frac{1 - \exp(-xu)}{1 - p \exp(-xu)} du$$

Where $1-p$ is the probability for an electron to be scattered diffusely at the surface.

This theory has been applied to iron of various purities to assess the surface effect on the damage rate determination and on the isochronal recovery curves under JANNUS conditions. As it is known that $1-p$ is close to zero for metal, this value has been used.

Size effect on the damage rate determination

Following the Fuchs-Sondheimer theory, we can write:

$$\left. \frac{d\rho^f}{dt} \right|_{t=0} = Q(x, t=0) \left. \frac{d\rho^b}{dt} \right|_{t=0} = Q(x, t=0) \rho_F \sigma_D \phi$$

Where ρ_F is the FP resistivity, σ_D the cross section of point defect creation and ϕ the ion flux.

This expression shows that an apparent cross section of Frenkel pairs creations in the thin foil be defined by $\sigma_D^f = Q(x, t=0) \sigma_D$.

The $Q(x, t=0)$ correction factors for iron samples 1 and 3μm thick and of various carbon contents prior irradiation are plotted in table 2. In this table, ρ_0 is the initial bulk resistivity of the iron (prior irradiation): The lower the value, the purer the iron. The value of $2 \cdot 10^{-11} \Omega m$ is the bulk resistivity of an ultra pure iron containing less than 1 ppm of carbon. As waited, the smaller the point defect concentration, the larger the correction. But for the ultra pure iron, the correction remains relatively small.

In addition, the correction has been calculated for a thin foil of 0.1μm, typically the thickness that can be obtained by vapour deposition of metal on rock salt [1]. In this last case the correction is very important.

Obviously, under irradiation the number density of point defect increases with fluence. The Q coefficient tends rapidly toward one.

Table 2: Q(x) function for irons of various purities

| | C atppm → | >1 | 15 | 66 |
|-------------------|---|-----|-----|-----|
| Thickness ↓ | ρ_0 ($10^{-11}\Omega\text{m}$) → | 2.0 | 9.3 | 34 |
| 1 μm | Q(x) | 2.1 | 1.3 | 1.1 |
| 3 μm | Q(x) | 1.4 | 1.1 | 1 |
| 0.1 μm | Q(x) | 9 | | |

Effect of the size correction on the recovery peak position

Assuming that the temperature is not increased step by step as in actual experiments but rather continuously ($T = \alpha t$), the temperature at peak T_p is given by:

$$\left. \frac{d^2 \rho^f}{dT^2} \right|_{T_p} = 0$$

Let us now consider for sake of simplification the hypothetical recovery peak associated with the elimination of one particular type of point defect on fix sink such as dislocations. It can be shown that T_p is solution of:

$$K D_0 \alpha \exp\left(-\frac{E_m}{kT_p}\right) \left(1 + xR(x)\right) - \frac{E_m}{kT_p^2} = 0,$$

Where K is a constant proportional to the dislocation density, E_m the migration energy of the considered defects, D_0 the frequency factor for diffusion, k the Boltzmann constant and:

$$R(x) = \frac{d \left\{ \ln \left[\frac{d\Phi(x)}{dx} \right] \right\}}{dx}$$

If $xR(x)$ is small compared to 1, the equation is the same as when there are no surface effects. In the opposite case, the temperature at peak must be corrected. To know if such a correction must be done in typical JANNUS conditions, $xR(x)$ has been calculated and plotted as a function of x (figure 1).

The correction factor $xR(x)$ for various sample thickness and various electrical resistivity at temperature just below the peak has been calculated (table 3).

We observe that the correction on the peak position can be significant if the number density of Frenkel pairs or carbon atoms remaining at peak is low, typically smaller than 10 appm. This is achieved only at the end of the recovery process for ultra pure iron. Indeed, at the begin of the recovery process i.e. at the level of the low temperature peaks, the number density of point defect introduced by irradiation is large enough permitting to avoid any size effect correction.

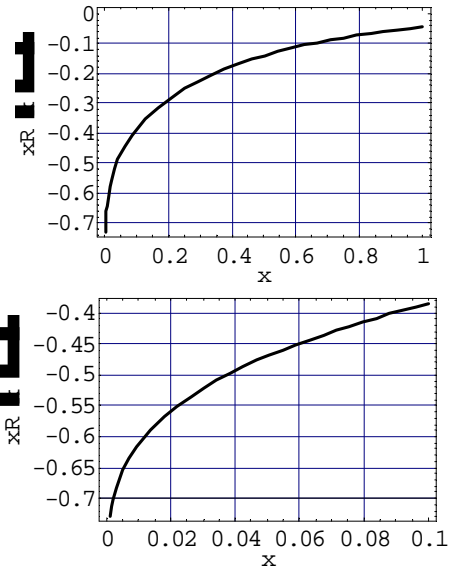


Figure 1: $xR(x)$ as a function of x

Table 3: Factor $xR(x)$ for various sample thickness and various bulk electrical resistivity

| | ρ^b ($10^{-11}\Omega\text{m}$) | 2.0 | 9.3 | 34 |
|-------------------|---------------------------------------|-------|-------|-------------|
| 1 μm | $xR(x)$ | -0.47 | -0.28 | -0.05 |
| 3 μm | $xR(x)$ | -0.36 | -0.10 | ≈ 0 |
| 0.1 μm | $xR(x)$ | -0.68 | | |

CONCLUSIONS

After a short review on the use of electrical resistivity measurements to obtain information about the damage rate under irradiation and the properties of induced point defects, we have considered the effect of the very small sample thickness compatible with the small range of ions in steels. We have shown that for typical ultra pure iron samples 1 and 3 mm thick, the correction induced by the scattering of conduction electrons on surfaces can be significant although moderate compared to 0.1 mm thick iron samples.

The remaining issue to carry out recovery electrical resistivity measurement in JANNUS is the preparation and the handling of such a small samples that is not a priori impossible but certainly tricky.

REFERENCES

[1] Averback R.S., Benedek, R., Merkel K.L., Phys. Rev. B, 18, 8 (1978) 4156
 [2] Dalla Torre J., Chu-Chun Fu, Willaime F., Barbu A. and Bocquet J.L., J. Nucl. Mat., 352, 1-3, (2006) 49

[3] Sondheimer E.H., Adv. Phys. 1, (1952) 1

[4] Takaki S., Fuss J., Kluger H., Dedek U., and Schultz H.,
Rad. Effects, 79 (1983) 87

[5] Fu C.C., Dalla Torre J., Willaime F. , Bocquet J.L. and
Barbu A., Nature materials, 4 (2005) 68

REPORTS AND PUBLICATIONS

[6] "Recovery follow-up by electrical resistivity or Infra-
Red (IR) spectroscopy of very thin samples irradiated
with the JANNUS multi-ion-beam facility", NT-SRMP-
07-12 (2007)

TASK LEADER

Alain BARBU

DEN/DMN/SRMP
CEA-Saclay
F-91191 Gif-sur-Yvette Cedex

Tel. : 33 1 69 08 86 88

Fax : 33 1 69 08 68 67

e-mail : alain.barbu@cea.fr

TW3-TTMA-001-D04
TW3-TTMA-002-D04

Task Title: SiC/SiC CERAMIC COMPOSITES AND DIVERTOR AND PLASMA FACING MATERIALS: FURIOSO IRRADIATION EXPERIMENT

INTRODUCTION

The main objective of these tasks is to determine the effects of high temperature neutron irradiation on physical and mechanical properties of SiC/SiC ceramic composites and tungsten alloys.

SiC_f/SiC ceramic composites are low activation materials and have good mechanical properties up to about 1000 °C. R&D work on these materials for advanced fusion devices has been going on over the past 2 decades. Recently, industrial scale productions have been achieved: in 2004 (2D material) and 2005 (3D material).

Tungsten alloys are candidate materials for structural applications in the high temperature region of the plasma facing components such as “high heat flux high temperature heat removal units” of helium cooled divertor concepts, which has recently gained more attention in the EU. The key issues for these materials include low fracture toughness, sensitivity to production history, but above all limited knowledge on the effects of irradiation on their mechanical properties.

Previous Activities

Samples of SiC_f/SiC composites and tungsten alloys have been prepared for irradiation in a common rig in the OSIRIS reactor (Furioso experiment, in position 64 SO). Irradiation will be performed at two temperatures of 600 and 1000°C to a dose of about 4.1·10²¹ n/cm² (equivalent of 4 dpa Fe), as shown in figure 1.

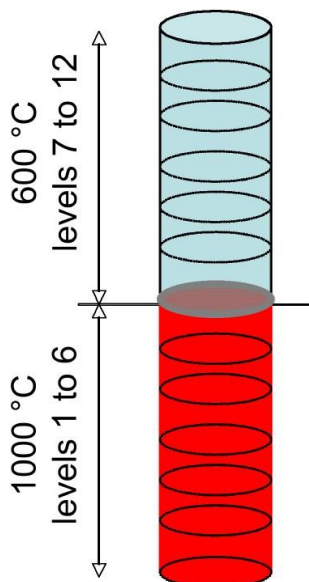


Figure 1: Schematic presentation of the Furioso Irradiation capsule

Specimens to be irradiated come from several European associations, as well as, the Japanese and the American partners. They include:

a) different nuances of SiC_f/SiC ceramic composites (2D and 3D), supplied by EFDA and manufactured in Europe by MAN Technology (Germany), plus a 2D-NITE material from Japan and four types of composites (TySA-CVI-Ti / HNLS-CVI-Ti / Hybrid-CVI / Reference) supplied by ORNL (U.S.). They are cut for mechanical testing (tensile and bend) and for thermal diffusivity measurements.

b) two types of tungsten alloys, one containing lanthanum oxide (W-1%La₂O₃) and other potassium addition (W-K). These materials will be irradiated as plate tensile specimens and Charpy-V sub-size (KLST) specimens (for bending tests).

In all:

154 specimens will be irradiated:

- 120 SiC_f/SiC composites
- 34 W alloys

16 thermocouples will monitor the temperatures.

14 dosimeters will record the irradiation doses.

2006 ACTIVITIES

During this period, fabrication of a rig mock-up, thermal calculations of specimens loading and the loading plan were finalized (figure 2). The plan was presented to all partners at the 7th IEA workshop held in Petten (Holland). Notice that in comparison with the earlier plan, there is a small modification in position of specimens in levels 6 and 7, for better temperature distribution. Also done in this period is preparation and submission of relevant documents to the safety authorities. Their permission to start the irradiation experiment is expected.

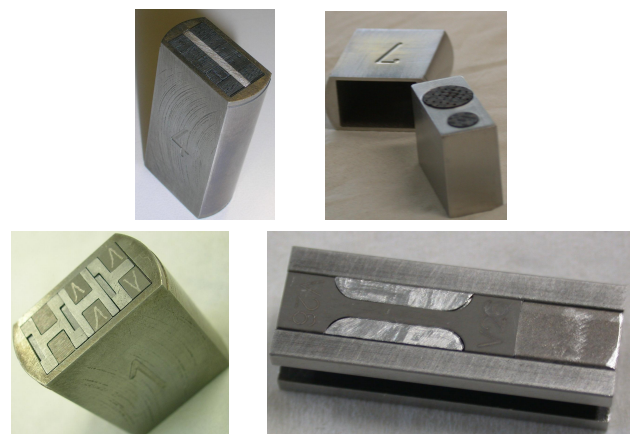


Figure 2: Specimen loading after thermal calculations

A few SiC_f/SiC diffusivity discs had traces of felt pen marking (see figure 3). Despite repeated cleaning according to the recommended procedures some of the markings were still visible. Most of these specimens were replaced with new ones except 2. All specimens have laser marking (see figure 3).



Figure 3: Specimen markings, on left traces of felt pen marking on diffusivity specimens, on right laser marking

A powerful furnace has been designed and manufactured, to guarantee the regulation and control of specimen's temperature during irradiation. A control box has been procured and installed next to the reactor (figure 4). The temperature inside the rig will be regulated with this box, using a flowing mixture of inert gas (helium-neon), inside and outside the sample holder.

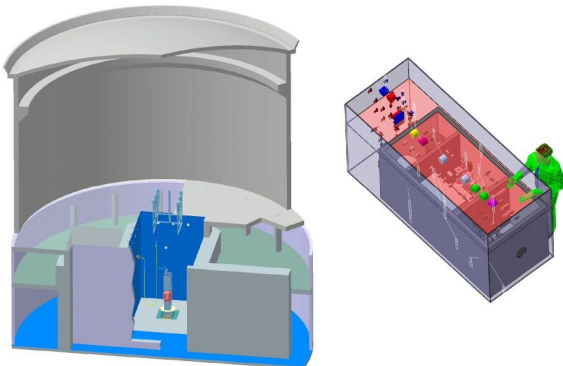


Figure 4: Schematic presentation of the control box procured and installed in 2006 next to the reactor. This box regulates the irradiation temperature inside the rig through flow of heated gases

Future Work

Pending approval of the safety authorities, start of the irradiation is scheduled in May 2007. Irradiation experiment will last for one year (May 2008) and final report issued in December 2008. Currently, negotiations are in progress with partners about dispatching of their specimens after irradiation.

CONCLUSIONS

All preliminary preparations for this very difficult high temperature irradiation experiment have been made. Irradiation experiment is expected to start in May 2007 and finish one year after.

REFERENCES

F. Tavassoli, C. Janis, A. Alamo, S. Bendotti, X. Palacin, 7th IEA Workshop on SiC/SiC for Fusion and First international Workshop on C&SiC composites for Advanced Fission, Sept. 18-20, 2006, Petten, The Netherlands

TASK LEADER

Farhad TAVASSOLI

DEN/DMN/DIR
CEA-Saclay
F-91191 Gif-sur-Yvette Cedex

Tel. : 33 1 69 08 60 21

Fax : 33 1 69 08 80 70

e-mail : tavassoli@cea.fr

**Task Title: MODELLING OF THE MECHANICAL BEHAVIOUR OF
ADVANCED 3D SiC_f/SiC COMPOSITES**

INTRODUCTION

The non linear elastic mechanical behaviour of SiC_f/SiC is governed by damage phenomena that take place at the scale of the components of the composite (fibre, matrix, interface). As a consequence, the most promising way to obtain a reliable behavioural model that can evolve with our knowledge of the material is to use multi-scale modelling. Such methods necessitate the knowledge of the thermodynamic and dissipation potentials for each component and a change scale method. The work performed in 2005 consisted in the implementation in the finite element software CAST3M of two new constitutive laws adapted to SiC_f/SiC composites. In 2006, the implementation of the GTFA (General Transformation Field Analysis) change scale method has started.

2006 ACTIVITIES

New Cast3M GIBIANE procedures were developed and tested in order to calculate the concentration and influence tensors necessary for the general transformation field analysis change scale method.

General transformation field analysis

The transformation field analysis proposed by Dvorak [1] and [2] links the local quantities (stress and strain in a sub-volume r , $\sigma_{\approx r}, \varepsilon_{\approx r}$) to the macroscopic ones (Σ, E) as follows:

$$\sigma_{\approx r} = B_{\approx r} : \Sigma + \sum_{s=1}^N F_{\approx rs} : \sigma_{\approx s}^{an} \quad (2.1)$$

and

$$\varepsilon_{\approx r} = A_{\approx r} : E + \sum_{s=1}^N D_{\approx rs} : \varepsilon_{\approx s}^{an} \quad (2.2)$$

where N is the number of sub-volumes. $\sigma_{\approx s}^{an}$ and $\varepsilon_{\approx s}^{an}$ are the microscopic eigenstresses and eigenstrains (stress-free strains) supposed to be uniform in each sub-volume s. $A_{\approx r}$ and $B_{\approx r}$ are respectively the mechanical strain and stress concentration tensors. $D_{\approx ss}, D_{\approx rs}, F_{\approx ss}$ and $F_{\approx rs}$ are respectively the self-induced (subscripts ss) and the transmitted (rs) eigenstrains and eigenstresses concentration tensors. If the elastic properties -of the sub-volume change (damage or temperature dependence), the tensors $A_{\approx r}, B_{\approx r}, D_{\approx ss}, D_{\approx rs}, F_{\approx ss}$ and $F_{\approx rs}$ are modified and should be reevaluated.

In order to avoid these expensive calculations, T. Pottier [3]) and J.L. Chaboche *et al.* [4] have generalised the aboveequations and introduced a generalised eigenstrain E^g . In addition to the plastic and thermal strain, this eigenstrain can take into account the variations of the elastic properties of the sub-phases with damage and/or temperature.

The two necessary scale change in SiC_f/SiC

The SiC_f/SiC structure implies that two scale changes are at least necessary to obtain the macroscopic material behaviour from the knowledge of the fibre and matrix ones. Figure 1 represents the chosen representative volume elements (RVE) at the mesoscopic scale (each sub-phase is an unidirectional plane) and at the microscopic scale (2 sub-phases: fibre and matrix). The concentration and influence tensor calculation procedures were developed by choosing estimates appropriated to the RVE for each scale change. The Mori-Tanaka estimate [2] was chosen for the micro-to-meso scale change and the Ross et al. estimate [5] was chosen for the meso-to-macro scale change.

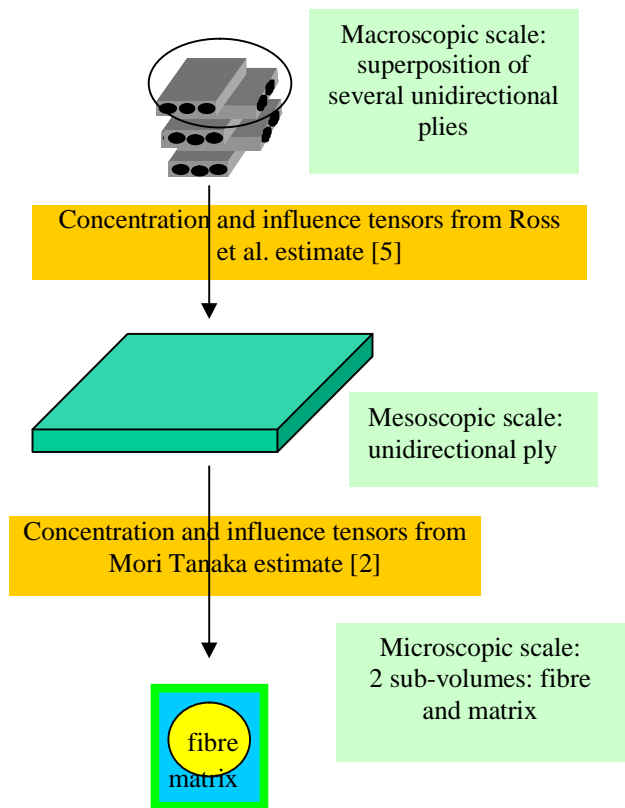


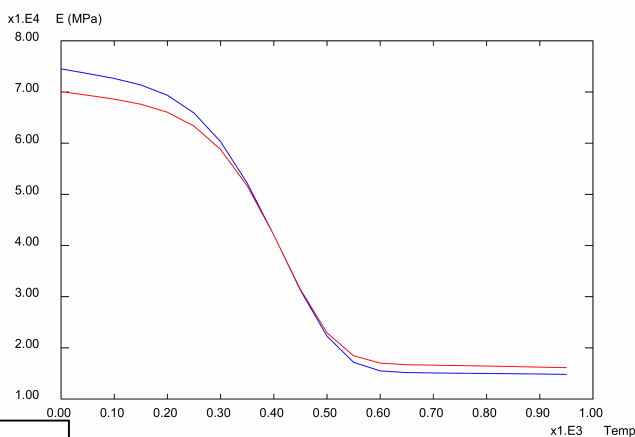
Figure 1: Different scales and associated estimates to model SiC_f/SiC from fibres and matrix behaviour

Tests of the new procedures

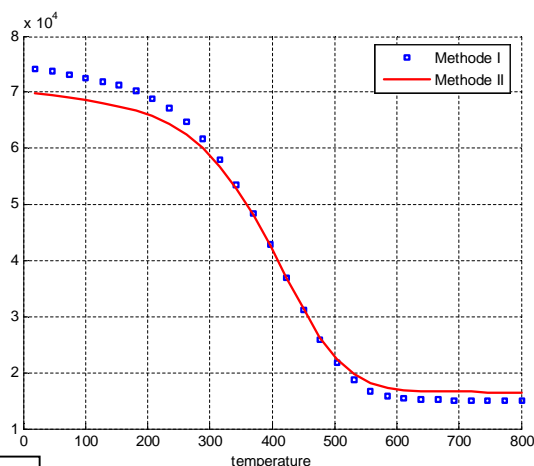
For example, some results issued from the tests of the procedures for the Mori-Tanaka estimate are illustrated in figure 2. The variation of the inverse ($1/M_{11}$) of the homogenised compliance tensor (M_{11}) of a fibrous composite is displayed as a function of temperature.

The variation of this component evaluated by a direct tensor calculation method is displayed in blue whereas the variation obtained from the GTFA method is displayed in red.

One may see that the GTFA method provides very good results in a wide temperature range around the reference temperature (400°C) at which the influence and concentration tensors are calculated only once. The graph of figure 2-a was obtained by a program provided by ONERA. It is identical to figure 2-b obtained using the GIBIANE procedures. This insures the good implementation of tensors calculations in Cast3M.



2-a



2-b

Figure 2: Inverse of the first term of the homogenised compliance tensor of a fibrous composite as a function of temperature using the Mori-Tanaka estimate

2-a graphic from Cast3m Gibiane procedures and 2-b graphic from Onera program. Blue curves correspond to direct calculations and red curves to GTFA method

CONCLUSIONS

GIBIANE procedures were developed in order to calculate the concentration and influence tensors for the GTFA method in the case of the Mori-Tanaka estimate, suitable for the micro-to-meso scale change, and Ross et al. estimate, suitable for the meso-to-macro scale change. It was verified that the calculations of the homogenised stiffness and thermal expansion for properties varying with temperature and damage were correctly performed using the GTFA method by comparing the results obtained from the newly implemented procedures and the ONERA results. These procedures were developed for the case of a two sub-phase material. It should be extended to more sub-phases in the future. The concentration and influence tensors will be introduced as material properties in the future. This is one of the necessary implementations in the scope to perform finite elements GFTA calculations for SiC_f/SiC modelling.

REFERENCES

- [1] G. Dvorak, Proc. Roy. Soc. Lond., vol. A437, (1992), pp. 311-327
- [2] G. Dvorak, Y. Benveniste, Proc. Roy. Soc. Lond., vol. A437 (1992), pp. 291-310
- [3] T. Pottier, 'Modélisation multiéchelles du comportement et de l'endommagement de composites à matrice métallique', Thèse de doctorat de l'Ecole nationale des ponts et chaussées, (1998)
- [4] J.L. Chaboche, S. Kruch, J.F. Maire, T. Pottier, Int. J. of Plasticity, vol. 17 (2001), pp. 411-439
- [5] A. Ross, J.L. Chaboche, L. Gélébart and J. Crépin, 'Multi-scale modeling of titanium aluminides', Int. J. of Plasticity, vol. 20, issues 4-5, April-May 2004, pp. 811-830

REPORTS AND PUBLICATIONS

- [6] C. Guerin, 'Multi-scale modelling for SiC_f/SiC composites, Preliminary considerations to an implementation in CAST3M'. CEA technical report DM2S/SEMT/LM2S/RT/04-001/A, January 2004
- [7] J.F. Maire and N. Carrère, 'Modélisation multiéchelles des composites SiC_f/SiC . Définition des potentiels thermodynamiques et de dissipation pour les différents constituants du composites SiC_f/SiC . ONERA Report RT 1/09795/DMSE – March 2005
- [8] N. Carrère and J.F. Maire, 'Modélisation multiéchelles des composites SiC_f/SiC . Fourniture des éléments nécessaires à l'implémentation d'une méthode de changement d'échelle pour les passages

micro-méso et méso-macro adaptée au SiC_f/SiC',
ONERA Report RT 2/09795/DMSE – March 2005

- [9] C. Rospars, N. Carrere, J.F. Maire and C. Guerin, 'Multi-scale modelling of the thermo-mechanical behaviour of SiC_f/SiC advanced composite. Definition of the constitutive laws and gathering of the data necessary for the implementation in CAST3M'. CEA technical report DM2S/SEMT/LM2S/RT/05-016/A
- [10] N. Carrère, J.F. Maire and F. Laurin, 'Modélisation multi-échelles des composites SiC_f/SiC. Fourniture des éléments nécessaires à l'implémentation d'une méthode de changement d'échelle pour les passages micro-méso et méso-macro adaptée au SiC_f/SiC' ONERA Report RT 2/09795/DMSE – December 2005
- [11] N. Carrère, J.F. Maire, F. Laurin, O. Fandeur and C. Guerin, 'Implementation in CAST3M of new models developed at ONERA for SiC_f/SiC composite. Comparison of CAST3M and Zebulon Results. Tests and application to the case of a divertor'. CEA technical report DM2S/SEMT/RT/05-034
- [12] C. Guerin, O. Fandeur, N. Carrère and J. F. Maire. 'Multi-scale modelling of SiC_f/SiC. 'CAST3M GIBIANE procedures for the calculation of the concentration and influence tensors for micro-meso and meso-macro scale changes'CEA technical report DM2S/SEMT/LM2S/RT/2006-038/A

TASK LEADER

Caroline GUERIN

DEN/DM2S/SEMT/LM2S
CEA-Saclay
F-91191 Gif-sur-Yvette Cedex

Tel. : 33 1 69 08 53 52
Fax : 33 1 69 08 86 84

e-mail : caroline.guerin@cea.fr